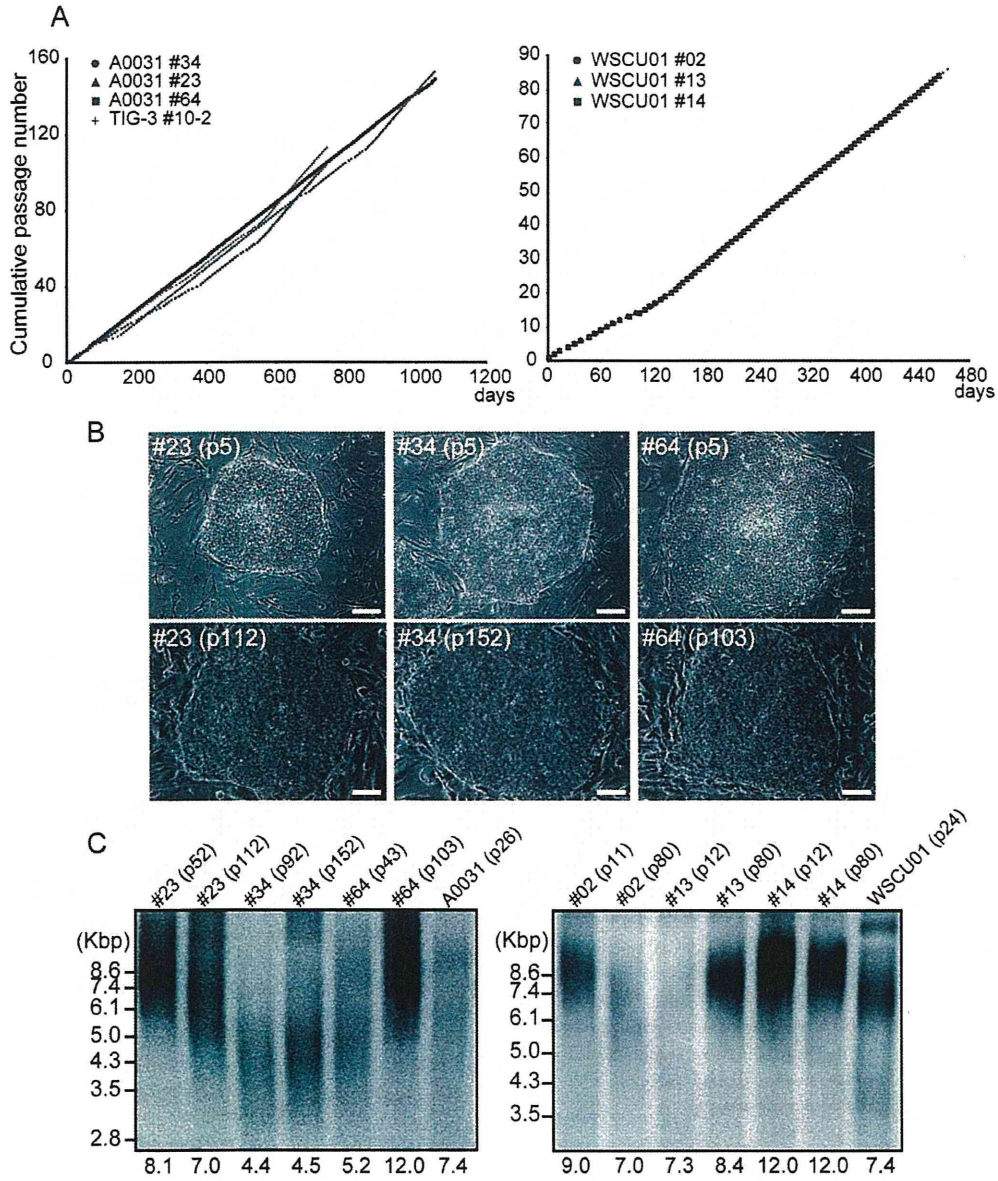

Figure 1. Infinite Proliferation of WS iPSCs after Long-Term Culture. (A) Cumulative passage number for WS iPSCs. (B) Colony morphologies of A0031-derived WS iPSC clones in early and late passages. Bars = 100 μm. (C) TRF length analysis of WS iPSC clones in early and late passages.
doi:10.1371/journal.pone.0112900.g001

18), and the Animal Care and Use Committee of Chiba University (25–131). All recombinant DNA experiments were performed in strict conformance with the guidelines of the Institutional Recombinant DNA Experiment Safety Committee at Hiroshima University.

Results

Infinite proliferative potential of WS iPSCs after long-term culture

To determine whether reprogramming provides WS cells with infinite proliferative potential, we generated iPSCs from WS patient fibroblasts. Morphologically distinct colonies from parental cells emerged after transduction of Yamanaka factors using retroviruses and showed elevated alkaline phosphatase activity (Figures S1A and S1B). Colonies were picked up, and 6 WS iPSC lines were established using fibroblasts from 2 independent WS patients after several passages. In western blotting analysis using an anti-WRN antibody, WRN protein was not detected in WS iPSCs but was expressed in both normal fibroblasts and iPSCs (Figure S2A). Direct sequencing analysis of WS iPSCs identified compound heterozygous Mut4/Mut6 mutations in the *WRN* gene similar to those observed in parental cells, and the derivation of WS iPSCs from parental cells was confirmed by STR analysis (Figures S2B and S2C). Finally, the 6 WS iPSC lines #23, #34, and #64 from A0031 and #02, #13, and#14 from WSCU01 were successfully established.

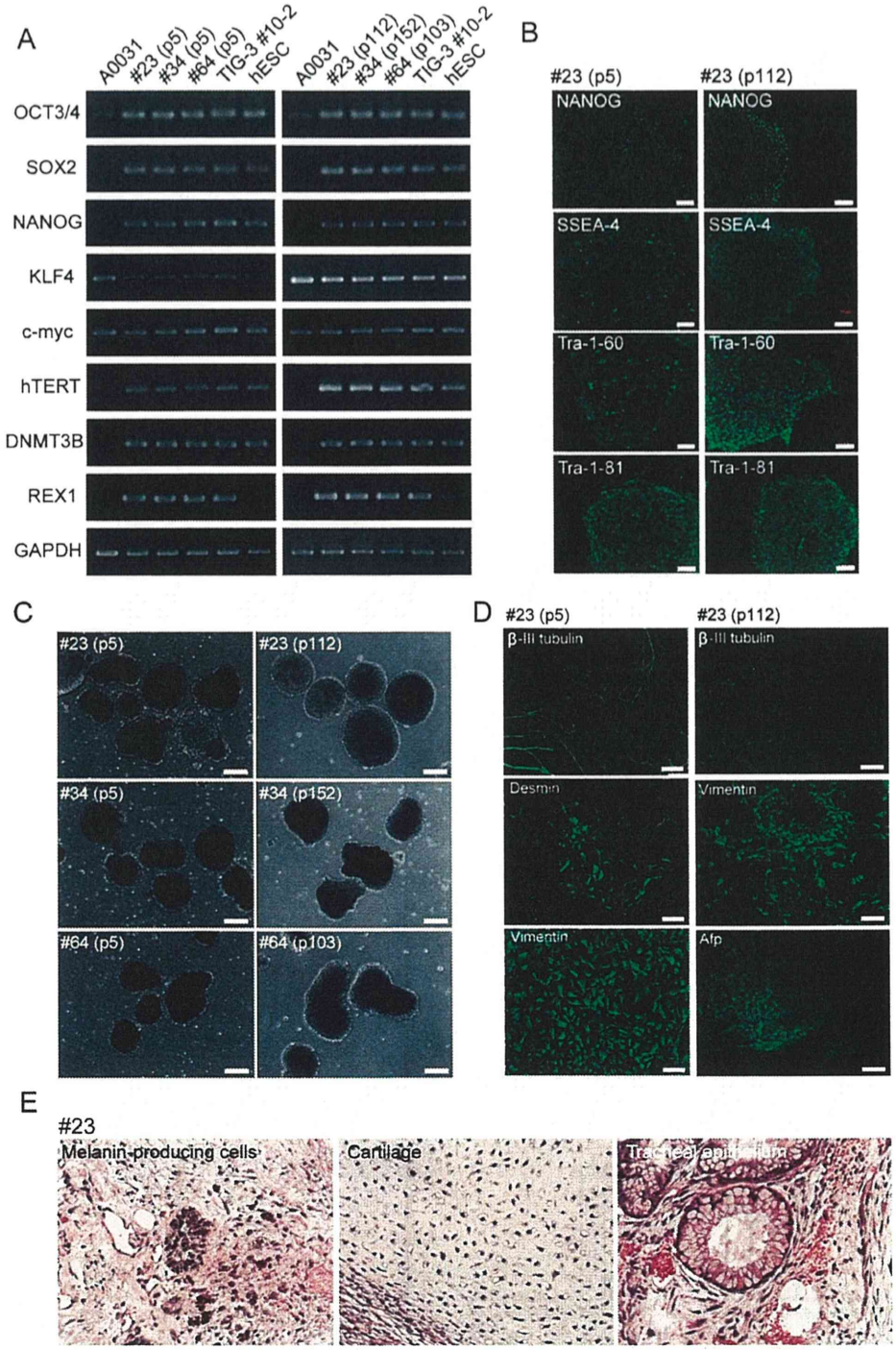

Figure 2. Sustained ESC-like characteristics of WS iPSCs after Long-Term Culture. (A) Expression of pluripotency genes in A0031-derived WS iPSC clones in early and late passages. (B) Expression of hESC markers in A0031-derived WS iPSC clone #23 in early and late passages. Bars = 100 μm. (C) EB formation in A0031-derived WS iPSC clones from early and late passages. Bars = 100 μm. (D) Immunocytochemical analysis of differentiation of EBs into 3 germ layers for A0031-derived iPSC clone #23 in early and late passages. β-III tubulin (ectoderm), desmin (mesoderm), vimentin (mesoderm and parietal endoderm), and α-fetoprotein (Afp, endoderm). Bars = 100 μm. (E) Hematoxylin and eosin histology of teratomas from A0031-derived iPSC clone #23. Formation of all 3 germ layers is shown including melanin-producing cells (ectoderm), cartilage (mesoderm), and tracheal epithelium (endoderm).
doi:10.1371/journal.pone.0112900.g002

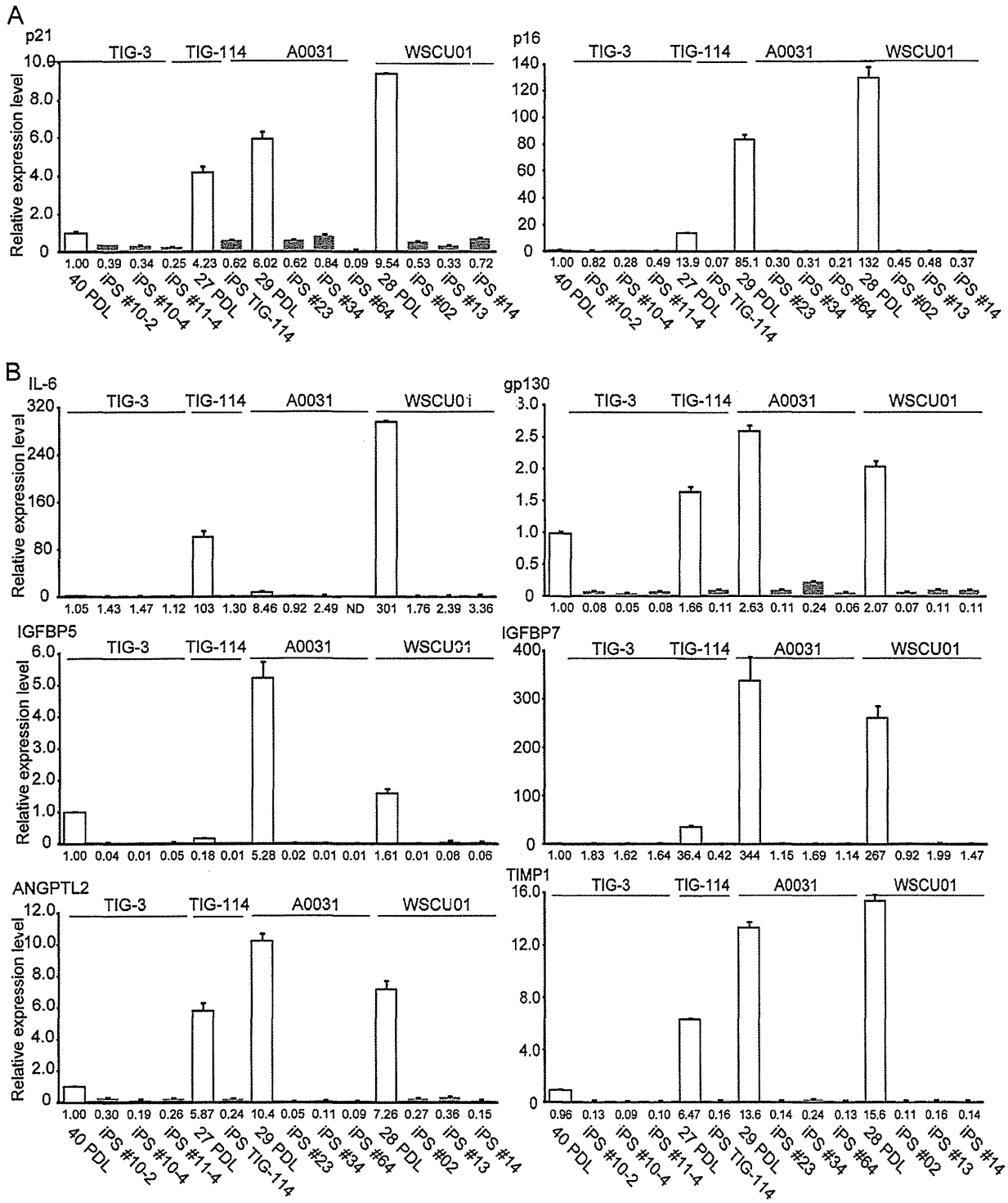

Figure 3. Suppression of Senescence-Associated Gene Expression in Reprogrammed WS iPSCs. (A) Expression of CDKI genes in parental fibroblasts and iPSCs. White columns show relative expression levels in the parental fibroblasts TIG-3, TIG-114, A0031, and WSCU01, and gray columns show those of their derived iPSC clones. Numbers under the horizontal axis in each graph show relative values in mRNA expression compared with that in TIG-3 fibroblasts. Values represent means of three technical replicates ± SD. (B) Expression of SASP genes in parental fibroblasts and iPSCs. Each graph is shown as in (A).
doi:10.1371/journal.pone.0112900.g003

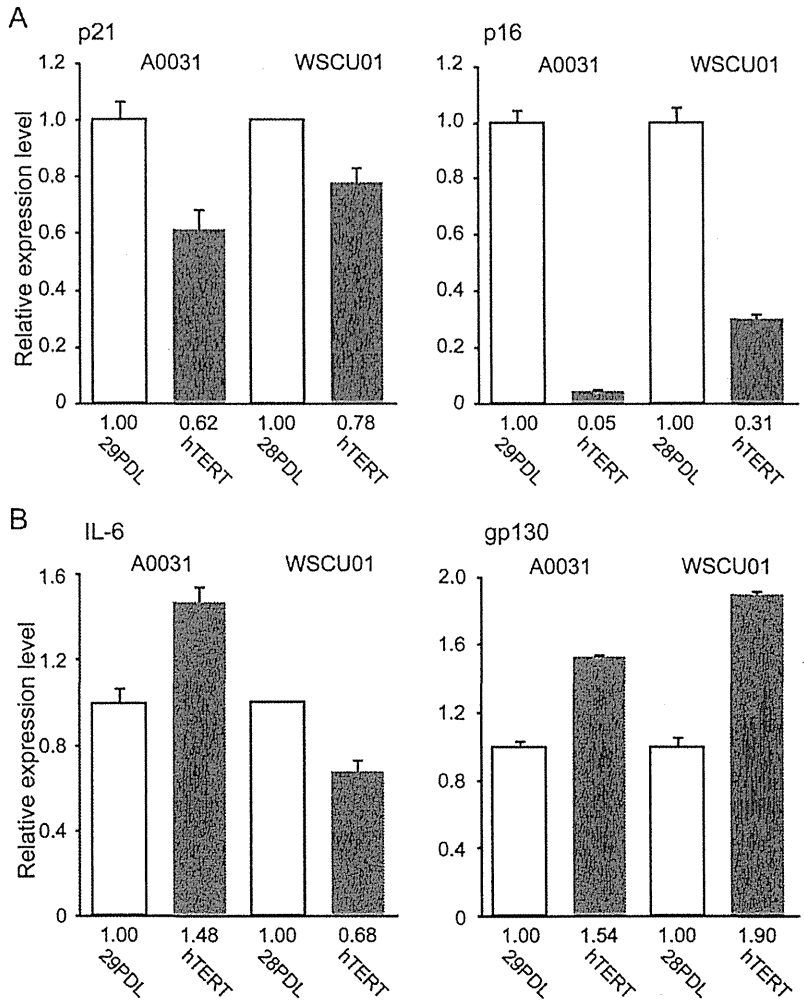

Figure 4. Reprogramming of the SASP gene loci is mediated by factors other than activated telomerase. (A) Expression of CDKI genes in WS fibroblasts and their hTERT-transduced derivatives. White columns show relative expression levels in A0031 and WSCU01 fibroblasts, and gray columns show those of their hTERT-transduced derivatives. Numbers under the horizontal axis in each graph show relative values in mRNA expression compared with that in parental fibroblasts. Values represent means of three technical replicates ± SD. (B) Expression levels of SASP genes in WS fibroblasts and their hTERT-transduced derivatives. Each graph is shown as in (C).
doi:10.1371/journal.pone.0112900.g004

WS iPSC lines from A0031 were cultured for 120 continuous passages over 2 years without morphological changes or loss of growth capacity (Figures 1A and 1B). Moreover, iPSC lines from WSCU01 proliferated for a year (Figures 1A and S1C). Average terminal restriction fragment (TRF) lengths in clones #23, #34, and #64 (A0031) were decreased, invariable, and increased during long-term culture, respectively, and similar telomere dynamics were observed in WSCU01-derived iPSC clones (Figure 1C).

Sustained ESC-like characters of WS iPSCs after long-term culture

To determine the persistence of ESC-like characteristics in WS iPSCs, we compared undifferentiated states and differentiation potentials between WS iPSCs from early and late passages. WS iPSC lines expressed pluripotency genes and hESC-specific surface markers during early passages (around p10), and during late passages (around p100; Figures 2A, 2B, S3 and S4). These iPSC lines also showed sustained formation of embryoid bodies and differentiation into 3 germ layers (Figures 2C, 2D, and S5). Furthermore, at around p50, WS iPSC lines generated teratomas that contained tissue structures of all 3 germ layers. These were consistent with those shown in normal iPSC lines after transplantation into the testes of SCID mice (Figures 2E and S6). Thus, reprogrammed WS fibroblasts acquired infinite proliferative potential, and the ESC-like characteristics of the resulting iPSCs were maintained for more than 2 years.

Suppression of senescence-associated gene expression in WS iPSCs after long-term culture

Global gene expression analysis using DNA chips showed pronounced similarities among pluripotent stem cells including WS iPSCs. However, marked differences between WS iPSC and WS fibroblasts were observed (Figure S7). Heat map analysis also showed a high analogy of global gene expression profiles in these

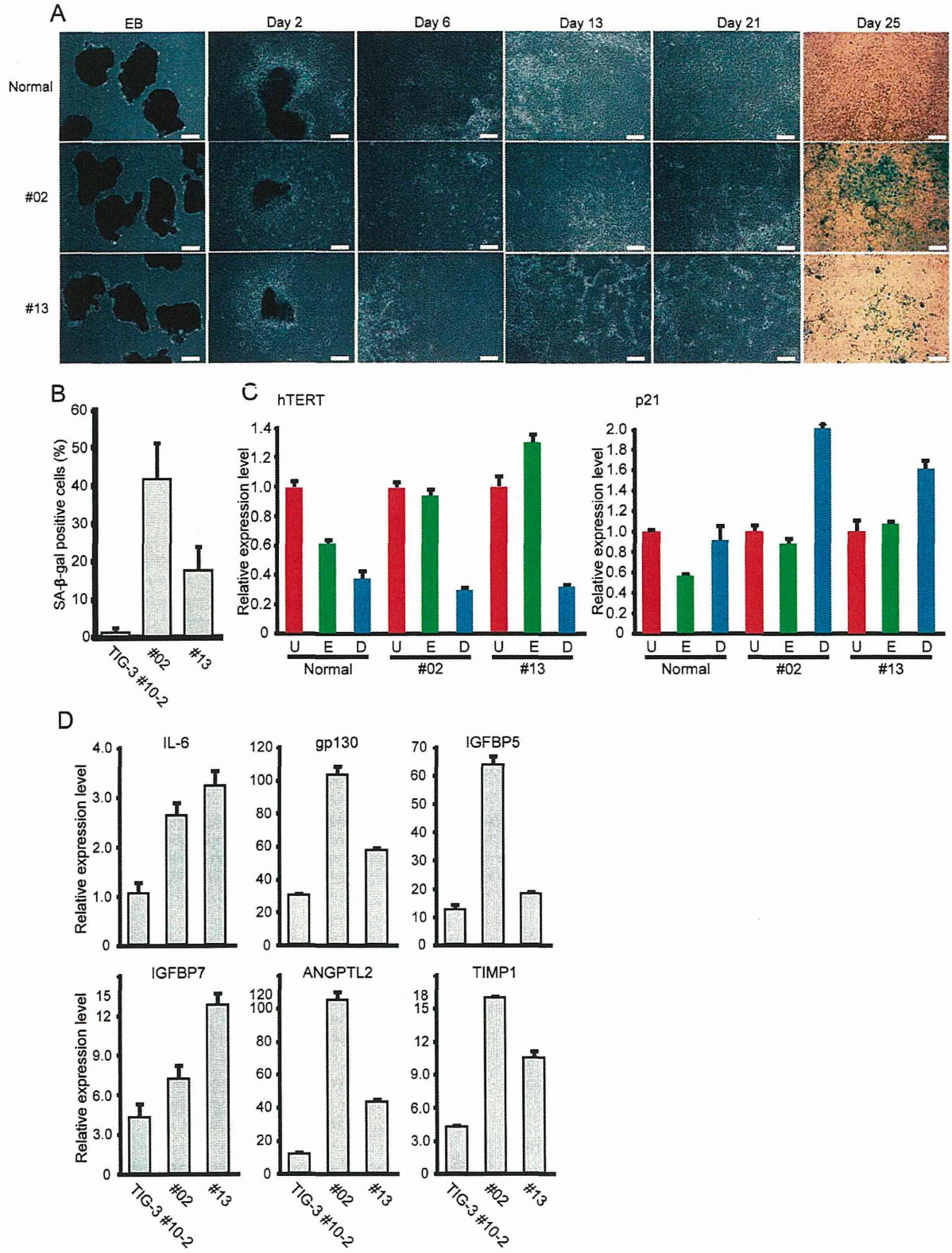

Figure 5. Recapitulation of Premature Senescence Phenotypes in Differentiated Cells from WS iPSCs. (A) Differentiation of EBs from normal (TIG-3) and WS (WSCU01 #02 and #13) iPSCs. Differentiated cells from WS iPSCs showed premature senescence. SA-β-gal staining was performed on day 25 of differentiation. Bars = 100 μm. (B) Percentage of senescent cells after 25 days of differentiation. SA-β-gal-positive cells were

counted in three randomly selected fields with 40× magnification. Values represent means of the three fields ± SD. (C) Expression of hTERT and p21 mRNAs in undifferentiated iPSCs ("U," red columns), EBs after 12 days of formation ("E," green columns), and differentiated cells after 25 days of differentiation ("D," blue columns). Values represent means of three technical replicates ± SD. (D) Expression of SASP genes in differentiated cells from normal (TIG-3) and WS (WSCU01 #02 and #13) iPSCs after 25 days of differentiation. Graphs shows fold changes relative to undifferentiated iPSCs. Values represent means of three technical replicates ± SD.
doi:10.1371/journal.pone.0112900.g005

pluripotent stem cell lines, but distinctly different profiles from those of WS fibroblasts (Figures S8A). Recent studies of aging have identified senescence-induced inflammatory and secretory factors that are collectively referred to as the senescence-associated secretory phenotype (SASP) and are the hallmarks of aging. It is widely accepted that age-associated inflammatory responses contribute to human aging mechanisms [26]. Accordingly, we observed downregulation of SASP secretory factors, including inflammatory cytokines, growth factors and MMPs, in both normal and WS iPSCs compared with WS fibroblasts (Figures S8B). Subsequently, we performed real-time qRT-PCR analysis using PDL-matched normal and patient fibroblasts, and their iPSC derivatives which were maintained in long-term culture. Although relative expression levels of the senescence-associated cyclin-dependent kinase inhibitor (CDKI) genes *p21Waf1/Cip1* and *p16INK4a* in normal fibroblasts correlated with the donor age, the expression levels of these genes were higher in WS fibroblasts than in normal fibroblasts, indicating that replicative senescence was prematurely induced in WS cells (Figure 3A). However, expression levels of these genes were significantly reduced in all iPSC clones from normal and WS cells (Figure 3A), suggesting that these gene loci are reprogrammed to the same degree in normal and WS iPSCs. Thus, we examined the expression of the typical SASP genes *IL-6* and *gp130* [27] and found higher expression levels in WS fibroblasts than in normal fibroblasts (Figure 3B). Moreover, expression levels of these genes drastically decreased in both normal and WS iPSCs compared with parental fibroblasts. Similarly, expression levels of the SASP genes *IGFBP5*, *IGFBP7*, *ANGPTL2*, and *TIMP1* ([28–31] were significantly decreased in both normal and WS iPSCs compared with parental fibroblasts (Figures 3B).

Reprogramming of the SASP gene loci is mediated by factors other than activated telomerase

WS fibroblasts were previously shown to bypass premature senescence following introduction of the telomerase gene *hTERT* [32], Similarly, the present WS cells bypassed premature replicative senescence, and hTERT allowed cell division for over 150 PDL in A0031 cells, and 40 PDL in WSCU01 cells compared with parental cells that became senescent at less than 30 PDL (Figures S9A and S9B). TRF length analysis showed that hTERT-expressing WS cells acquired longer telomeres during passages than parental cells (Figures S9C). To examine whether the expression of hTERT was sufficient to suppress the upregulation of aging-associated genes in WS cells, we compared expression levels of CDKI and SASP genes between WS fibroblasts and their hTERT-expressing derivatives. Whereas a decline in p21waf1/cip1 and p16INK4a mRNA expression was observed in hTERT-expressing cells (Figure 4A), IL-6 and gp130 expression was not suppressed following the introduction of hTERT, suggesting that reprogramming of the SASP gene loci is mediated by factors other than activated telomerase (Figure 4B). The present data show complete suppression of premature senescence phenotypes in WS cells using transcription factor-induced reprogramming and suggest that persistence of the undifferentiated state and pluripotency are crucial for reversing the aging process.

Recapitulation of premature senescence phenotypes in differentiated cells from WS iPSCs

To establish cell lineages that prematurely senesced, EBs consisting of equal numbers of iPSCs maintained in long-term culture were differentiated in serum-containing medium. Differentiated cells from WS iPSC-derived EBs were outgrown less rapidly than those from normal iPSC-derived EBs (Figure 5A, Day 2). These cells exhibited flat and enlarged morphology (Figure 5A, Day 6, 13, and 21) and became positive for SA-β-gal staining (Figure 5A, Day 25, and Figure 5B). Whereas expression levels of hTERT were downregulated equally in differentiated cells from normal and WS iPSCs, p21 mRNA was more highly induced in differentiated cells from WS iPSCs than those from normal iPSCs (Figure 5C). Expression levels of the SASP genes were also significantly increased in differentiated cells from WS iPSCs

Table 1. Results of chromosome analysis of WS iPSC clones and their parenral cells.

Cell lines	Numbers of cells analyzed by G-banding	Numbers of cells analyzed by M-FISH	Karyotypes
A0031	20 (13/7)	ND	46,XY,del(8)(q22q24)/46,XY,t(1;14)(p34.1;q13),t(4;7)(p15.2;q22),del(8)(q22q24)
iPS#23	20	10	46,XY,t(1;14)(p34.1;q13),t(4;7)(p15.2;q22),del(8)(q22q24),der(21)t(17;21)(?;q22.3)
iPS#34	20	10	46,XY,t(1;14)(p34.1;q13),t(4;7)(p15.2;q22),del(8)(q22q24)
iPS#64	20	10	46,XY,t(1;14)(p34.1;q13),t(4;7)(p15.2;q22),del(8)(q22q24),der(19)t(2;19)(?;p13.3)
WSCU01	20	ND	46,XY,normal
iPS#02	20	10	47,XY,+del(20)(p?)
iPS#13	20	10	46,XY,normal
iPS#14	20	10	46,XY,normal

Abbreviations: t, translocation; del, deletion; der, derivative chromosome; p, short arm; q, long arm.
doi:10.1371/journal.pone.0112900.t001

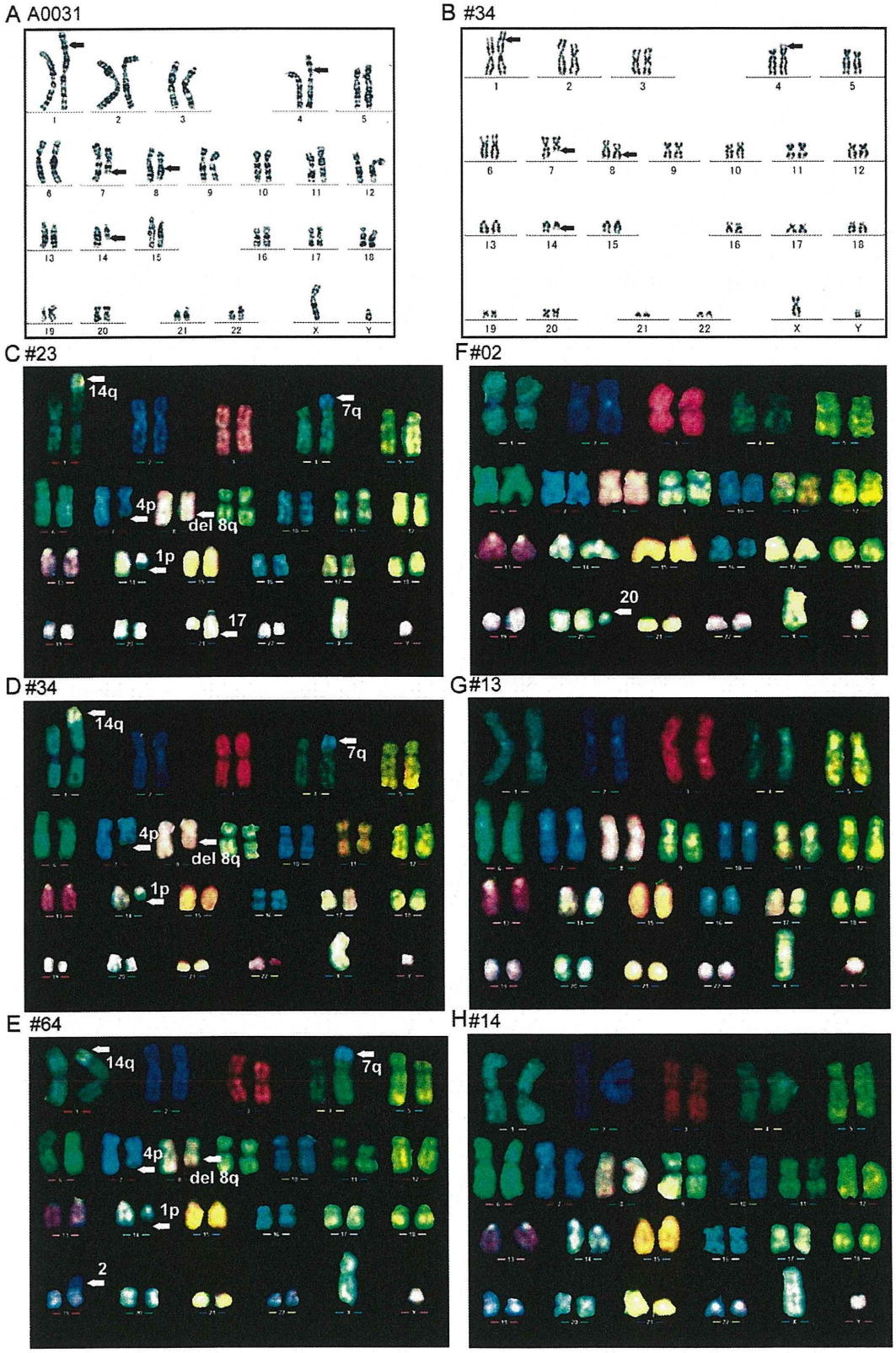
A A0031
B #34
C #23
14q
7q
4p
del 8q
1p
17
F #02
20
D #34
14q
7q
4p
del 8q
1p
G #13
E #64
14q
7q
4p
del 8q
1p
2
H #14

Figure 6. Karyotype Analysis of WS iPSCs. Chromosomal profiles of G-band analysis. (A) Parental A0031 fibroblast and (B) A0031-derived iPSC clone #34. Arrows indicate translocation breakpoints. Chromosomal profiles of M-FISH analysis. A0031-derived iPSC clones (C) #23, (D) #34, and (E) #64 and WSCU01-derived iPSC clones (F) #02, (G) #13, and (H) #14. Arrows indicate translocation breakpoints or an extra chromosome.
doi:10.1371/journal.pone.0112900.g006

compared with those from normal iPSCs (Figure 5D). These results demonstrated recapitulation of premature senescence phenotypes with downregulation of hTERT in differentiated cells from WS iPSCs.

Karyotype analysis of WS iPSCs

WS is characterized by genomic instability, and gene translocation events have been observed during culture of patient-derived cells [33]. Because reprogramming of somatic cells and subsequent maintenance of iPSCs involves extensive cell division, WS iPSCs may acquire additional chromosomal abnormalities. Thus, we compared chromosomal profiles of long-term cultured WS iPSC clones with those of parental WS fibroblasts by karyotype analysis. The subsequent G-banding stain and multicolor fluorescence *in situ* hybridization (M-FISH) analysis are summarized in Table 1.

Chromosomal profiles of parental A0031 WS fibroblasts showed mosaicism with the following abnormal karyotypes: 46, XY with a deletion in 8q and 46, XY with a deletion in 8q along with reciprocal translocations between 1p and 14q, and 4p and 7q (Figure 6A). These karyotypes support previous observations of chromosomal instability in WS cells [33]. Whereas, 1 of the derived iPSC clones (#34) had the same chromosomal profile as its parent cells (Figures 6B and 6D), the other 2 A0031-derived iPSC clones (#23 and #64) had the translocations 21q and 19p, respectively, in addition to those of the parental karyotype (Table 1, Figures 6C and 6E). Moreover, whereas parental WSCU01 fibroblasts and 2 of their derived iPSC clones (#13 and #14) had normal karyotypes (Table 1, Figures 6G and 6H), the remaining iPSC clone #02 carried the abnormal karyotype 47 (XY with an additional aberrant chromosome derived from chromosome 20; Table 1, Figure 6F).

The observation that 3 of 6 WS iPSC clones had the same karyotypes as their parental cells after approximately 100 passages suggests that karyotypes of WS cells are stabilized following reprogramming.

Discussion

In this study, we demonstrated that WS fibroblasts could be reprogrammed into iPSCs using Yamanaka factors, and the resulting iPSCs showed unlimited proliferative capacity that was sufficient for self-renewal over a period of 2 years. WS iPSCs also exhibited undifferentiated states and differentiation potential after long-term culture. Subsequently, we showed that WS iPSCs maintain immortality and ESC-like characteristics that indicate corrected telomere dysfunction following reprogramming of WS cells. Although WRN was not essential for generation of iPSCs, WRN helicase may protect genome integrity by mechanism other than the maintenance of telomere in iPSCs.

TRF length analysis indicated that WS iPSC lines maintained telomere with size variation in each clone. It is known that human iPSCs derived from normal somatic cells showed varied telomere length, and variation of telomere length among human iPSC clones is thought to partly depend on acquired telomerase activity associated with their reprogrammed states [34,35]. Therefore, variation of telomere length observed among WS iPSC clones would be due to clonal variation in telomerase activity rather than telomere dysfunction associated with *WRN* deficiency.

Normal human iPSCs are known to acquire genomic instability with a high incidence of additions, deletions and translocations [36,37]. In contrast, chromosomal aberrations are frequently caused by telomere dysfunctions in WS fibroblasts following the induction of cell cycle progression [11]. Nonetheless, the present data show unexpected maintenance of chromosomal profiles in WS iPSC clones during long-term culture for more than 100 passages although half of these clones acquired additional chromosomal abnormalities. Previously, the introduction of hTERT reduced the chromosomal aberrations in cells from WS patients [11]. In agreement, the present data indicate endogenous hTERT expression in WS iPSCs, but not in parental fibroblasts, suggesting that reprogramming suppresses chromosomal instability in WS cells by reactivating telomerase.

Previous studies show that WS fibroblasts express inflammatory cytokines [38] and WS is associated with inflammatory conditions such as atherosclerosis, diabetes and osteoporosis [39–43]. The present data indicate that both CDKI and SASP genes are prematurely induced in WS fibroblasts compared with PDL-matched normal fibroblasts. However, expression levels of these genes were completely suppressed in WS iPSCs to the same degree observed in normal iPSCs. In contrast, hTERT did not suppress SASP genes in WS fibroblasts, as shown by previous study [44], although a decline in p21waf1/cip1 and p16INK4a mRNAs was observed. Taken together, these observations suggest that pluripotency-associated transcription factor-induced reprogramming reverses the aging process in both normal and WS cells. Furthermore, differentiated cells from EBs of long-term cultured WS iPSCs showed premature senescence phenotypes, thus demonstrating that WS iPSCs stably maintained their potential to recapitulate premature senescence phenotypes during differentiation over the long term. In addition, embryoid body-mediated iPSC differentiation recapitulated premature senescence phenotypes in WS iPSCs, suggesting that it would provide a simple and rapid way to identify cell lineages affected in WS.

In the present study, we demonstrated the potential of WS iPSCs to proliferate infinitely and differentiate into various cell types, which could be used to provide patient cells in large quantities over the long term. Because WS-specific iPSCs may be differentiated into multiple cell types, their experimental use may resolve the major pathogenic processes of WS for which cell types available from patients are usually limited to lymphocytes and/or fibroblasts. The present technologies may also be used to develop cell transplantation therapies for WS patients using gene-corrected patient cells. The present observations indicate that WS iPSCs may be a powerful tool for understanding normal aging and the pathogenesis of WS.

Supporting Information

Figure S1 Generation of WS iPSCs. (A) Generation of iPSCs. Normal (TIG-3) and Werner syndrome (A0031 and WSCU01) fibroblasts are shown in the left panels, and emergence of morphologically distinct ESC-like colonies from parental cells is shown in the right panels. (B) Alkaline phosphatase activity of ESC-like colonies derived from TIG-3 and A0031 fibroblasts. (C) Colony morphologies of WSCU01-derived WS iPSC clones in early and late passages. Bars = 100 μm.
(EPS)

Figure S2 Evidences that WS iPSCs were derived from patients. (A) Western blot analysis of WRN helicase protein in WS iPSCs. (B) Direct sequencing analysis identified compound heterozygous mut.4/mut.6 mutations in WS iPSCs. Mut.4 is a C to G substitution at the splice-donor site bordered by exon 26, as shown by an arrow in the illustration of the double-strand base sequence. Obtained pherograms show antisense peak shapes. A peak corresponding to mut.4 in normal TIG-3 fibroblast shows a single "C," whereas the WS iPSC clone #34 from A0031 fibroblasts gave double peaks showing "G" in addition to "C." Mut.6 is a T to C substitution in exon 9. A peak corresponding to mut.6 in normal cells showed a single "C," whereas WS iPSC gave double peaks showing "T" in addition to "C." C, blue; G, black; T, red; A, green. (C) STR analysis of A0031-derived iPSC clone #34, showing that iPSC clone #34 was derived from the parental A0031 fibroblasts.
(EPS)

Figure S3 Expression of pluripotency genes in WSCU01-derived WS iPSC clones in early and late passages.
(EPS)

Figure S4 Expression of hESC markers in WS iPSCs in early and late passages. A0031-derived clones #34, and #64, and WSCU01-derived clones #02, #13, and #14 are shown. Bars = 100 μm.
(EPS)

Figure S5 Immunocytochemistry for differentiation of embryoid bodies into 3 germ layers for WS iPSCs in early and late passages. A0031-derived clones #34, and #64, and WSCU01-derived clones #02, #13, and #14 are shown. Bars = 100 μm.
(EPS)

Figure S6 Hematoxylin and eosin histology of teratomas derived from iPSCs. Hematoxylin and eosin histology of teratomas derived from iPSCs. The normal TIG-3 fibroblast-derived clone #10-2, A0031-derived clones #34, and #64, and the WSCU01-derived clone #02 are shown. Formation of all 3 germ layers is shown with melanin-producing cells and glial tissue (ectoderm), cartilage (mesoderm) and intestinal epithelia. Glands are lined by columnar epithelia and tracheal epithelium (endoderm).
(EPS)

Figure S7 Figure Scatter plots comparing gene expression profiles.
(EPS)

Figure S8 Analysis of senescence-associated gene expression in iPSCs. (A) Heat map analysis of WS iPSC #34 and parental WS A0031 fibroblasts, normal TIG-3 fibroblast-derived iPSCs, and hESC; 3277 probes with >5-fold differences in expression between A0031 fibroblast and WS iPSC were included in the heat map. (B) Heat map analysis of the gene profiles of secreted protein probes with >2-fold differences in expression between A0031 fibroblasts and the 3 pluripotent stem cell lines WS iPSC, TIG-3 iPSC, and hESC.
(EPS)

Figure S9 hTERT bypassed premature replicative senescence of WS fibroblasts. (A) Morphologies of growing normal TIG-3 fibroblasts, and A0031 and WSCU01 WS fibroblasts. WS fibroblasts showed premature senescence. SA-β-gal staining was performed for WSCU01 (lower). Bars = 100 μm. (B) Cumulative population doubling levels for hTERT-expressing WS cells. (C) TRF lengths of A0031 fibroblasts and their TERT-transduced derivatives.
(EPS)

Table S1
(EPS)

Table S2
(EPS)

Acknowledgments

We are grateful to Miho Kusuda-Furue (National Institute of Biomedical Innovation), Hidenori Akutsu (National Center for Child Health and Development) and Haruhiko Koseki (RCAI RIKEN) for their help, encouragement and suggestions. We also thank M. K. F and Bunsyo Shiotani for the critical review of draft manuscripts, and the Analysis Center of Life Science, Natural Science Center for Basic Research and Development of Hiroshima University for processing microarray data.

Author Contributions

Conceived and designed the experiments: AS. Performed the experiments: AS HK KZ YS YK MO MO HK TS KH HS YI KH YK. Analyzed the data: AS YK MO MO TS KH HS YI KH YK. Contributed reagents/materials/analysis tools: MG MT KY SY KF HT. Wrote the paper: AS MG. Final approval of the version to be published: AS HT.

References

1. Goto M, Miller RW, Ishikawa Y, Sugano H (1996) Excess of rare cancers in Werner syndrome (adult progeria). Cancer Epidemiol Biomarkers Prev 5: 239–246.
2. Goto M (2000) Werner's syndrome: from clinics to genetics. Clin Exp Rheumatol 18: 760–766.
3. Salk D, Au K, Hoehn H, Martin GM (1981) Effects of radical-scavenging enzymes and reduced oxygen exposure on growth and chromosome abnormalities of Werner syndrome cultured skin fibroblasts. Hum Genet 57: 269–275.
4. Yu CE, Oshima J, Fu YH, Wijsman EM, Hisama F, et al. (1996) Positional cloning of the Werner's syndrome gene. Science 272: 258–262.
5. Oshima J, Yu CE, Piussan C, Klein G, Jabkowski J, et al. (1996) Homozygous and compound heterozygous mutations at the Werner syndrome locus. Hum Mol Genet 5: 1909–1913.
6. Goto M, Imamura O, Kuromitsu J, Matsumoto T, Yamabe Y, et al. (1997) Analysis of helicase gene mutations in Japanese Werner's syndrome patients. Hum Genet 99: 191–193.
7. Matsumoto T, Imamura O, Yamabe Y, Kuromitsu J, Tokutake Y, et al. (1997) Mutation and haplotype analyses of the Werner's syndrome gene based on its genomic structure: genetic epidemiology in the Japanese population. Hum Genet 100: 123–130.
8. Shimamoto A, Sugimoto M, Furuichi Y (2004) Molecular biology of Werner syndrome. Int J Clin Oncol 9: 288–298.
9. Rossi ML, Ghosh AK, Bohr VA (2010) Roles of Werner syndrome protein in protection of genome integrity. DNA Repair (Amst) 9: 331–344.
10. Crabbe L, Verdun RE, Haggblom CI, Karlseder J (2004) Defective telomere lagging strand synthesis in cells lacking WRN helicase activity. Science 306: 1951–1953.
11. Crabbe L, Jauch A, Naeger CM, Holtgreve-Grez H, Karlseder J (2007) Telomere dysfunction as a cause of genomic instability in Werner syndrome. Proc Natl Acad Sci U S A 104: 2205–2210.
12. Takahashi K, Yamanaka S (2006) Induction of pluripotent stem cells from mouse embryonic and adult fibroblast cultures by defined factors. Cell 126: 663–676.
13. Takahashi K, Tanabe K, Ohnuki M, Narita M, Ichisaka T, et al. (2007) Induction of pluripotent stem cells from adult human fibroblasts by defined factors. Cell 131: 861–872.
14. Yu J, Vodyanik MA, Smuga-Otto K, Antosiewicz-Bourget J, Frane JL, et al. (2007) Induced pluripotent stem cell lines derived from human somatic cells. Science 318: 1917–1920.
15. Aoi T, Yae K, Nakagawa M, Ichisaka T, Okita K, et al. (2008) Generation of pluripotent stem cells from adult mouse liver and stomach cells. Science 321: 699–702.
16. Stadtfeld M, Hochedlinger K (2010) Induced pluripotency: history, mechanisms, and applications. Genes Dev 24: 2239–2263.

17. Okita K, Yamanaka S (2011) Induced pluripotent stem cells: opportunities and challenges. Philos Trans R Soc Lond B Biol Sci 366: 2198–2207.
18. Stadtfeld M, Maherali N, Breault DT, Hochedlinger K (2008) Defining molecular cornerstones during fibroblast to iPS cell reprogramming in mouse. Cell Stem Cell 2: 230–240.
19. Cheung HH, Liu X, Canterel-Thouennon L, Li L, Edmonson C, et al. (2014) Telomerase protects werner syndrome lineage-specific stem cells from premature aging. Stem Cell Reports 2: 534–546.
20. Batista LF, Pech MF, Zhong FL, Nguyen HN, Xie KT, et al. (2011) Telomere shortening and loss of self-renewal in dyskeratosis congenita induced pluripotent stem cells. Nature 474: 399–402.
21. Goto M, Ishikawa Y, Sugimoto M, Furuichi Y (2013) Werner syndrome: A changing pattern of clinical manifestations in Japan (1917~2008). Biosci Trends 7: 13–22.
22. Morita S, Kojima T, Kitamura T (2000) Plat-E: an efficient and stable system for transient packaging of retroviruses. Gene Ther 7: 1063–1066.
23. Amps K, Andrews PW, Anyfantis G, Armstrong L, Avery S, et al. (2011) Screening ethnically diverse human embryonic stem cells identifies a chromosome 20 minimal amplicon conferring growth advantage. Nat Biotechnol 29: 1132–1144.
24. Ohtaki K, Sposto R, Kodama Y, Nakano M, Awa AA (1994) Aneuploidy in somatic cells of in utero exposed A-bomb survivors in Hiroshima. Mutat Res 316: 49–58.
25. Debacq-Chainiaux F, Erusalimsky JD, Campisi J, Toussaint O (2009) Protocols to detect senescence-associated beta-galactosidase (SA-betagal) activity, a biomarker of senescent cells in culture and in vivo. Nat Protoc 4: 1798–1806.
26. Goto M (2008) Inflammaging (inflammation + aging): A driving force for human aging based on an evolutionarily antagonistic pleiotropy theory? Biosci Trends 2: 218–230.
27. Salama R, Sadaie M, Hoare M, Narita M (2014) Cellular senescence and its effector programs. Genes Dev 28: 99-114.
28. Kojima H, Kunimoto H, Inoue T, Nakajima K (2012) The STAT3-IGFBP5 axis is critical for IL-6/gp130-induced premature senescence in human fibroblasts. Cell Cycle 11:
29. Wajapeyee N, Serra RW, Zhu X, Mahalingam M, Green MR (2008) Oncogenic BRAF induces senescence and apoptosis through pathways mediated by the secreted protein IGFBP7. Cell 132: 363–374.
30. Tabata M, Kadomatsu T, Fukuhara S, Miyata K, Ito Y, et al. (2009) Angiopoietin-like protein 2 promotes chronic adipose tissue inflammation and obesity-related systemic insulin resistance. Cell Metab 10: 178–188.
31. Gilbert LA, Hemann MT (2010) DNA damage-mediated induction of a chemoresistant niche. Cell 143: 355–366.
32. Wyllie FS, Jones CJ, Skinner JW, Haughton MF, Wallis C, et al. (2000) Telomerase prevents the accelerated cell ageing of Werner syndrome fibroblasts. Nat Genet 24: 16–17.
33. Salk D, Au K, Hoehn H, Stenchever MR, Martin GM (1981) Evidence of clonal attenuation, clonal succession, and clonal expansion in mass cultures of aging Werner's syndrome skin fibroblasts. Cytogenet Cell Genet 30: 108–117.
34. Mathew R, Jia W, Sharma A, Zhao Y, Clarke LE, et al. (2010) Robust activation of the human but not mouse telomerase gene during the induction of pluripotency. FASEB J 24: 2702–2715.
35. Vaziri H, Chapman K, Guigova A, Teichroeb J, Lacher M, et al. (2010) Spontaneous reversal of the developmental aging of normal human cells following transcriptional reprogramming. Regen Med 5: 345–363.
36. Taapken SM, Nisler BS, Newton MA, Sampsell-Barron TL, Leonhard KA, et al. (2011) Karotypic abnormalities in human induced pluripotent stem cells and embryonic stem cells. Nat Biotechnol 29: 313–314.
37. Martins-Taylor K, Nisler BS, Taapken SM, Compton T, Crandall L, et al. (2011) Recurrent copy number variations in human induced pluripotent stem cells. Nat Biotechnol 29: 488–491.
38. Kumar S, Vinci JM, Millis AJ, Baglioni C (1993) Expression of interleukin-1 alpha and beta in early passage fibroblasts from aging individuals. Exp Gerontol 28: 505–513.
39. Murano S, Nakazawa A, Saito I, Masuda M, Morisaki N, et al. (1997) Increased blood plasminogen activator inhibitor-1 and intercellular adhesion molecule-1 as possible risk factors of atherosclerosis in Werner syndrome. Gerontology 43 Suppl 1: 43–52.
40. Yokote K, Hara K, Mori S, Kadowaki T, Saito Y, et al. (2004) Dysadipocytokinemia in werner syndrome and its recovery by treatment with pioglitazone. Diabetes Care 27: 2562–2563.
41. Rubin CD, Zerwekh JE, Reed-Gitomer BY, Pak CY (1992) Characterization of osteoporosis in a patient with Werner's syndrome. J Am Geriatr Soc 40: 1161–1163.
42. Davis T, Kipling D (2006) Werner Syndrome as an example of inflamm-aging: possible therapeutic opportunities for a progeroid syndrome? Rejuvenation Res 9: 402–407.
43. Goto M, Sugimoto K, Hayashi S, Ogino T, Sugimoto M, et al. (2012) Aging-associated inflammation in healthy Japanese individuals and patients with Werner syndrome. Exp Gerontol 47: 936–939.
44. Choi D, Whittier PS, Oshima J, Funk WD (2001) Telomerase expression prevents replicative senescence but does not fully reset mRNA expression patterns in Werner syndrome cell strains. FASEB J 15: 1014–1020.

Cancer Science
Japanese Cancer Association JCA
Open Access

DSE-FRET: A new anticancer drug screening assay for DNA binding proteins

Toru Miyagi,[1,2] Bunsyo Shiotani,[1] Ryuya Miyoshi,[1] Takuya Yamamoto,[1] Takanori Oka,[3] Kazuo Umezawa,[4] Takahiro Ochiya,[5] Mikihisa Takano[6] and Hidetoshi Tahara[1]

[1]Department of Cellular and Molecular Biology, Graduate School of Biomedical & Health Science, Hiroshima University, Hiroshima; [2]Japanese Red Cross Kanto-koshinetsu Block Blood Center, Tokyo; [3]Wakunaga Pharmaceutical Co. Ltd., Hiroshima; [4]Department of Molecular Target Medicine Screening, Aichi Medical University School of Medicine, Aichi; [5]Division of Molecular and Cellular Medicine, National Cancer Center Research Institute, Tokyo; [6]Department of Pharmaceutics and Therapeutics, Graduate School of Biomedical & Health Sciences, Hiroshima University, Hiroshima, Japan

Key words

Antineoplastic agents, dehydroxymethylepoxyquinomicin, DNA-binding proteins, fluorescence resonance energy transfer, NF-κB

Correspondence

Hidetoshi Tahara, 1-2-3 Kasumi, Minami-ku, Hiroshima 734-8553 Japan.

Tel: +81-82-257-5290; Fax:+81-82-257-5294

E-mail: toshi@hiroshima-u.ac.jp

Funding information

Ministry of Education, Culture, Sports, Science and Technology of Japan

Received January 8, 2014; Revised April 3, 2014; Accepted April 9, 2014

Cancer Sci **105** (2014) 870–874

doi: 10.1111/cas.12420

Nuclear factor-κB (NF-κB) is a key regulator of cancer progression and the inflammatory effects of disease. To identify inhibitors of DNA binding to NF-κB, we developed a new homogeneous method for detection of sequence-specific DNA-binding proteins. This method, which we refer to as DSE-FRET, is based on two phenomena: protein-dependent blocking of spontaneous DNA strand exchange (DSE) between partially double-stranded DNA probes, and fluorescence resonance energy transfer (FRET). If a probe labeled with a fluorophore and quencher is mixed with a non-labeled probe in the absence of a target protein, strand exchange occurs between the probes and results in fluorescence elevation. In contrast, blocking of strand exchange by a target protein results in lower fluorescence intensity. Recombinant human NF-κB (p50) suppressed the fluorescence elevation of a specific probe in a concentration-dependent manner, but had no effect on a non-specific probe. Competitors bearing a NF-κB binding site restored fluorescence, and the degree of restoration was inversely correlated with the number of nucleotide substitutions within the NF-κB binding site of the competitor. Evaluation of two NF-κB inhibitors, Evans Blue and dehydroxymethylepoxyquinomicin ([−]-DHMEQ), was carried out using p50 and p52 (another form of NF-κB), and IC_{50} values were obtained. The DSE-FRET technique also detected the differential effect of (−)-DHMEQ on p50 and p52 inhibition. These data indicate that DSE-FRET can be used for high throughput screening of anticancer drugs targeted to DNA-binding proteins.

DNA-binding proteins such as transcription factors play key roles in normal biological processes and in development of disease. Nuclear factor-κB (NF-κB) is a DNA-binding protein involved in inflammation and tumorigenesis, and thus inhibition of NF-κB signaling is a potential target for cancer therapy; however, there are few direct inhibitors of NF-κB binding to DNA. In general, DNA-binding proteins are attractive therapeutic targets,[1,2] but conventional methods for detecting protein–DNA binding, such as a gel-shift assay,[3] DNA footprinting assay,[4,5] and ELISA,[6] are laborious and time-consuming, and thus not amenable to combinatorial screening.

Fluorescent-based homogeneous methods have been exploited for detection of sequence-specific protein–DNA binding,[7–9] including use of the split probe "molecular beacon" method in a FRET-based assay.[7] In this method, a DNA fragment containing a protein binding site is split into two parts in the middle of the site. One part is labeled with a donor fluorophore and the other has an acceptor fluorophore. Fluorescence resonance energy transfer between the two fluorophores is produced as a result of protein-dependent association of the split DNA fragments. The molecular beacon is simple in principle and is cost-effective. However, probe designs are complicated for three reasons. First, protein-independent association of the two DNA molecules may occur. Second, fluorophores can disturb protein–DNA binding or fluorescence can be changed by the protein because the fluorophores are introduced into nucleotides proximal to the protein binding site. Finally, nicks in the associated DNA fragment can influence protein binding because proteins interact with the phosphate backbone, in addition to the bases. Fluorescence-based DNA footprinting can overcome these drawbacks.[8,9] This method is based on a DNA-binding protein protecting its target DNA against exonuclease III digestion. However, the method requires careful quality control of exonuclease III activity to obtain stable data, and the half-life of the protein–DNA complex must be long compared with the time required for the exonuclease III reaction.

The Holliday junction is a four-way DNA structure that is the central intermediate in homologous recombination. Branches of the structure migrate spontaneously *in vitro* as a result of strand exchange between two DNA molecules, and DNA-binding proteins including the histone octamer, p53, TRF1, and TRF2 suppress the strand exchange.[10–12] We have found that NF-κB also suppresses this strand exchange *in vitro*. Based on these findings, we developed a new homoge-

neous method for detection of protein–DNA binding and screening of drugs targeting DNA-binding proteins.

Materials and Methods

Oligonucleotides. The following probe oligonucleotides were made for NF-κB-DSE-FRET (F, 6FAM; D, DABCYL; lowercase letters, single-stranded tail; underline, NF-κB binding site): 5′-FAG TTG AGG GGA CTT TCC CAG GCG ACT CAC TAT AGG Cgg tgt ctc gct cgc-3′ (NF-01F), 5′-AGT TGA GGG GAC TTT CCC AGG CGA CTC ACT ATA GGc acc aca cca ttc cc-3′ (NF-13), 5′-ggg aat ggt gtg gtG CCT ATA GTG AGT CGC CTG GGA AAG TCC CCT CAA CTD-3′ (NF-14D), 5′-gcg agc gag aca ccG CCT ATA GTG AGT CGC CTG GGA AAG TCC CCT CAA CT-3′ (NF-02). To prepare probes, 0.5 μM of each oligonucleotide was mixed in annealing buffer (10 mM HEPES-NaOH [pH 7.9], 50 mM KCl, 0.1 mM EDTA), denatured for 2 min at 95°C, and then cooled gradually to allow annealing. Duplexes were stored at 4°C and diluted with binding buffer (10 mM HEPES–NaOH [pH 7.9], 50 mM KCl, 0.1 mM EDTA, 2.5 mM DTT, 10% glycerol, 0.05% Nonidet P40) before use. Oligonucleotides were purchased from Japan Bio Services (Saitama, Japan). All other chemicals were reagent grade or better and were obtained from Wako (Tokyo, Japan).

Protein preparation and DNA binding assay. The GST-fusion recombinant human NF-κB proteins (p50, p52) were expressed and purified[13] and glutathione was removed by dialysis. In general, DNA-binding experiments were carried out in the following manner: 5 μL NF-D1 (consisting of NF-01F and NF-14D) and 5 μL protein in binding buffer were incubated in a 96-well (half-area) microplate for 30 min at room temperature. Next, 40 μL NF-D2 (consisting of NF-02 and NF-13) was added and allowed to incubate for another 60 min at room temperature. Fluorescence was measured at 535 nm after excitation at 485 nm using an EnVision microplate reader (Perkin-Elmer, Waltham, MA, USA). In experiments with inhibitor, 0.5 μL inhibitor, 5 μL NF-D1, and 4.5 μL protein in binding buffer were incubated before addition of 40 μL NF-D2.

To obtain an IC_{50}, the following equation was solved using the "solver" add-on in Microsoft Excel:

$$Y = A + \frac{B - A}{1 + \left(\frac{X}{IC_{50}}\right)^C} \quad (1)$$

where Y is the observed fluorescence, X is the inhibitor concentration, A is the lowest fluorescence, B is the highest fluorescence, and C gives the largest absolute value of the slope of the curve.

S/B was obtained by the following formula:

$$S/B = \frac{A}{P} \quad (2)$$

where A is the mean fluorescence of four wells in the absence of protein and P is the mean florescence of four wells in the presence of protein.

Z'-factors were obtained as follows:

$$Z'\text{-factor} = 1 - \frac{3 \times SD_A + 3 \times SD_P}{A - P} \quad (3)$$

where A is the mean fluorescence value of four wells without protein, P is the mean florescence of four wells with protein, SD_A is the standard deviation of A, and SD_P is the standard deviation of P.

Results

The principle of DSE-FRET is illustrated in Figure 1. Two partially double-stranded DNA probes, named D1 and D2, are used. Each probe has a double-stranded region containing a protein binding site and two single-stranded tails. One strand of D1 is labeled with a fluorophore at the 5′-end and the other is labeled with a quencher at the 3′-end. The fluorophore and quencher are placed at the same end of the double-stranded region; therefore, the fluorescence of the fluorophore is quenched. The tails of D1 are complementary to those of D2, so that D1 hybridizes with D2 to form a four-way structure. As the double-stranded regions of the two probes have identical sequences, the junction of the structure migrates spontaneously, followed by irreversible dissociation to give two fully double-stranded duplexes. In other words, strand exchange occurs between D1 and D2. As a result, the quencher-labeled strand of D1 is exchanged for its non-labeled counterpart in D2; therefore, fluorescence is restored. DNA-binding proteins bind to the duplex and block strand exchange, thereby suppressing the fluorescence elevation.

To illustrate the method, we attempted to detect the NF-κB (p50) interaction with DNA. Nuclear factor-κB plays a pivotal role in the coordinated transcription of multiple inflammatory genes and is a probable drug target.[14–16] Two probes, NF-D1 and NF-D2, were prepared to test quantitative detection of p50 binding to DNA. Their double-stranded regions are identical and include an NF-κB binding sequence, d(GGGACTTTCC). These probes interact with each other through their single-stranded tails and are then involved in a strand exchange reaction. Each strand of NF-D1 was labeled with 6FAM and DABCYL at the double-stranded terminus. NF-D1, various concentrations of recombinant p50, and NF-D2 were mixed in a half-area 96-well microplate and changes in fluorescence were measured. Time courses of these changes are shown in Figure 2. The fluorescence signal of NF-D1 increased rapidly within 30 min after addition of NF-D2 and was fivefold higher than that of NF-D1 alone at 60 min in the absence of p50. Fluorescence elevation was suppressed in a p50 concentration-dependent manner by half at 40 nM p50 and almost completely at 320 nM p50.

Duplex NF-01F02, which consists of NF-01F and NF-02, was prepared as a positive control as a completely exchanged product. Fluorescence of NF-01F02 was not affected by p50 (Fig. 2). We then optimized the concentrations of NF-D1 and

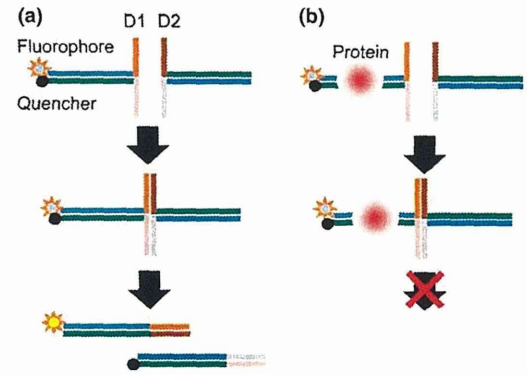

Fig. 1. Principles of the DSE-FRET assay. (a) In the absence of target protein, strand exchange between D1 and D2 will occur and fluorescence will be elevated. (b) In the presence of target protein, strand exchange will not occur and fluorescence will remain quenched.

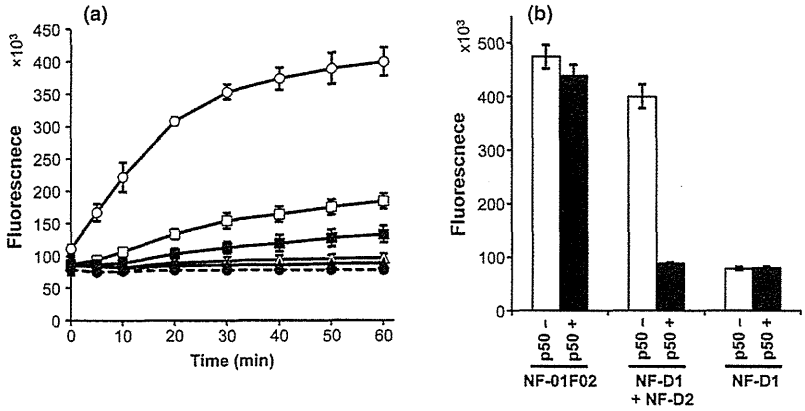

Fig. 2. Dose-dependent suppression of DNA strand exchange by p50. (a) Five microliters of 40 nM NF-D1 was mixed with 5 μL of 0 nM (open circles), 400 nM (open squares), 800 nM (closed squares), 1600 nM (open triangles), or 3200 nM (closed triangles) p50 and incubated for 30 min. Then, 40 μL of 10 nM NF-D2 was added and fluorescence was measured; thus, the final concentrations of p50 were 0, 40, 80, 160, and 320 nM, respectively. Closed circles with a dotted line represent NF-D1 alone. (b) Fluorescence at 60 min for a positive control completely exchanged product (NF-01F + NF-02, named NF-01F02), an exchanged product (NF-D1 + NF-D2), and an unexchanged product (NF-D1 alone) with 0 or 320 nM p50. Error bars represent ±3 SD (n = 4).

NF-D2. Varied concentrations of NF-1D (1, 2, and 4 nM) were mixed with twofold or fourfold amounts of NF-2D in the presence (40 nM) or absence of p50. As shown in Table 1, the combination of 2 nM NF-D1 and 8 nM NF-D1 showed the highest Z'-factor (0.93). S/B values (ratio in the absence to presence of p50) were 1.9–2.3 and were not influenced by the DNA concentration. Therefore, we used 2 nM NF-D1 with 8 nM NF-D2 in the following assays.

We examined the specificity of the assay by using double-stranded competitor DNA. NF-cpt1 is a specific competitor DNA bearing a NF-κB binding site. NF-cpt2, NF-cpt3, NF-cpt4, and NF-cpt5 are non-specific competitors with one to four nucleotides substituted in the NF-κB binding site. NF-cpt1 completely restored the fluorescence suppressed by p50 (Fig. 3). The restoration level decreased as the number of substituted nucleotides in non-specific competitors increased and NF-cpt5, with four substituted nucleotides, had little effect on p50 binding. For further evaluation of specificity, we prepared non-specific probes, NFs-D1 and NFs-D2, with nucleotide substitutions as in NF-cpt5. The fluorescence signal of the nonspecific probes was not affected by p50 (Fig. 3). Hence, we concluded that p50 suppressed strand exchange in a sequence-specific manner.

A 10-point dose–response experiment with Evans Blue (EB) was also carried out. One hundred μM Evans Blue inhibits NF-κB binding to DNA by EMSA and has been suggested to bind non-covalently to the p50 DNA binding region by molecular modeling.[17] In DSE-FRET, 10 μM EB showed little effect on p50, but 30 μM EB inhibited p50 completely (Fig. 4). Evans Blue also inhibited p52 in a similar fashion. The IC_{50} values of EB for p50 and p52 inhibition were 12.9 and 12.8 μM, respectively. We also showed that our method can be used for evaluation of an uncompetitive inhibitor, (−)-DHMEQ, which binds covalently to a specific Cys residue of Rel family proteins to inhibit their DNA binding.[18,19] We detected an inhibitory effect of (−)-DHMEQ on p50 and p52 by DSE-FRET (Fig. 5). As shown previously,[19] (−)-DHMEQ was less potent against p52 (IC_{50} 62.5 μM) compared to p50 (IC_{50} 8.8 μM).

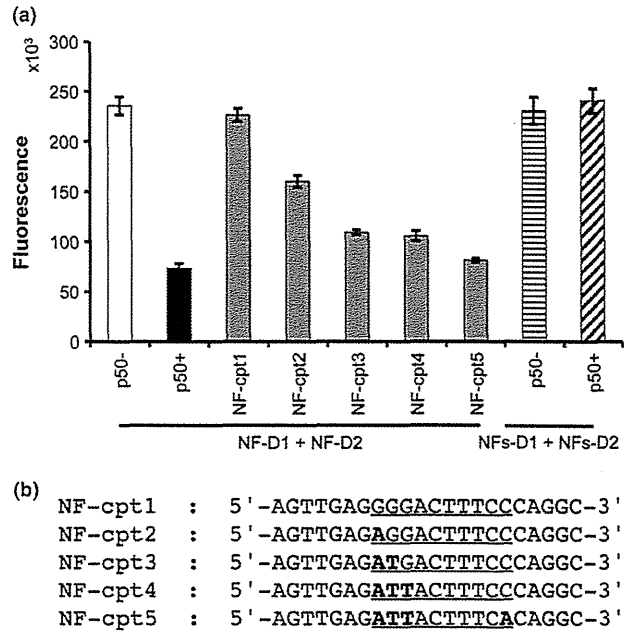

Fig. 3. Specificity of DSE-FRET. (a) 2.5 μL of 2000 nM competitor was mixed with 2.5 μL of 800 nM p50 and incubated for 30 min. Then, 5 μL of 20 nM NF-D1 was added and incubated for a further 30 min. Finally, 40 μL of 10 nM NF-D2 was added and fluorescence was measured: NF-D1 and NF-D2 without p50 (white bar), without competitor (black bar), and with competitors (gray bars). Horizontally and diagonally striped bars indicate non-specific probes (NFs-D1 + NFs-D2) without and with p50, respectively. (b) Sequences of the competitor upper strand are shown: underline, nuclear factor-κB (NF-κB) binding site; bold type, substituted nucleotide in binding site. Error bars represent ±3 SD (n = 4).

Table 1. Optimization of probe concentration

D1 (nM)	D2 (nM)	*S/B*	Z′-factor
4	8	1.9	0.77
2	4	2.3	0.90
2	8	2.2	0.93
1	2	2.1	0.83
1	8	1.9	0.82

Discussion

The DSE-FRET technique can detect protein–DNA interaction quantitatively and specifically using a simple procedure; just mix and measure. It detected p50 binding with a high Z′-factor and a dose–response analysis was carried out with two types of inhibitor (EB and (−)-DHMEQ). Moreover, the differential effect of (−)-DHMEQ on p50 and p52 was well displayed. Yamamoto *et al.* found that (−)-DHMEQ inhibited

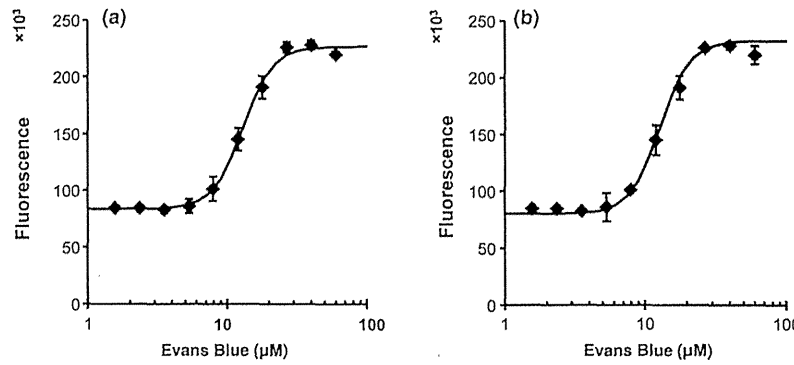

Fig. 4. Dose–response of Evans Blue (EB). Half a microliter of various concentrations of EB was mixed with 4.5 μL of 890 nM p50 (a) or p52 (b) and incubated for 30 min. Then, 5 μL of 20 nM NF-D1 was added and incubated for a further 30 min. Finally, 40 μL of 10 nM NF-D2 was added and fluorescence was measured. Horizontal axes show the concentration of EB in incubations with protein and NF-D1. Error bars represent ±SD (n = 4).

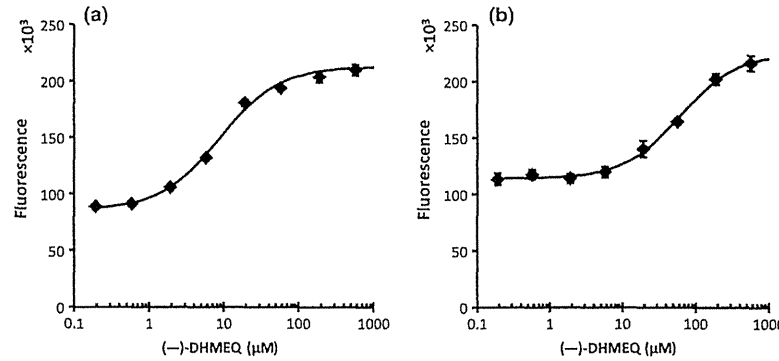

Fig. 5. Dose–response of dehydroxymethylepoxyquinomicin ([−]-DHMEQ). Half a microliter of various concentrations of (−)-DHMEQ was mixed with 4.5 μL of 440 nM p50 (a) or p52 (b) and incubated for 30 min. Then, 5 μL of 20 nM NF-D1 was added and incubated for a further 30 min. Finally, 40 μL of 10 nM NF-D2 was added and fluorescence was measured. Horizontal axes show the concentrations of (−)-DHMEQ in incubations with protein and NF-D1. Error bars represent ±SD (n = 4).

p50 more strongly than p52 in EMSA analysis.[19] The same preference of the inhibitor was shown by DSE-FRET, with the IC_{50} for inhibition of p50 being sevenfold lower than that for p52. However, the amount of (−)-DHMEQ required to inhibit the proteins differed between the two methods. A (−)-DHMEQ concentration fourfold that of p50 (80–20 μM) inhibited protein binding completely in EMSA,[19] whereas a (−)-DHMEQ concentration 44-fold that of p50 (8.8–0.2 μM) was required to inhibit half of the p50 binding in DSE-FRET. In contrast, inhibition of (−)-DHMEQ to p52 was shown only by DSE-FRET. The basis for these differences is unclear.

As a stable and homogeneous assay, DSE-FRET is particularly useful for high throughput screening. These features are particularly important for initial screening of a huge combinatorial library. Although we carried out the assay in a 96-well (half area) format, a 384-well format can be used with appropriate specialized equipment. The probes used in DSE-FRET consist of a double-stranded moiety and two single-stranded tails. Inadequate intra- and intermolecular hybridization of tails interferes with appropriate formation of a four-way junction and markedly reduces the efficiency of strand exchange. Thus, we evaluated 13 tails before choosing the tails used here. These tails were also confirmed to not have protein binding sequences using the transcription factor analysis tool TFSearch (version 1.3 online, http://mbs.cbrc.jp/research/db/TFSEARCH.html). Therefore, these tails may be applicable universally. The double-stranded moiety should have a sequence that allows protein binding, but is otherwise not restricted in sequence. Taken together, these features make design of a probe for DSE-FRET as easy as that for EMSA.

To our knowledge, this is the first report to show that NF-κB blocks spontaneous strand exchange. Several proteins, including histone octamer, p53, TRF1, and TRF2, have also been found to block strand exchange.[10–12] However, this blockage can be explained based on particular features of these proteins: thus, the histone octamer forms a large protein–DNA complex and the other proteins have junction-binding activity. Panyutin and Hsieh[20] found that spontaneous strand exchange is also blocked by a mismatch, which suggests that this process may be blocked easily by a small energy barrier.

In this paper, we established a novel technique to identify NF-κB inhibitors as anticancer drugs. Nuclear factor-κB is a desirable target for therapy in various cancers and inflammatory diseases.[21,22] In most cancer cells, NF-κB is localized in the nucleus and is constitutively active. This persistent activity of nuclear NF-κB protects cancer cells from apoptotic cell death. Therefore, anticancer drug targeting of NF-κB may have great therapeutic value by inhibiting cell growth or increasing the sensitivity of conventional chemotherapy. We believe that the DSE-FRET assay will be a powerful tool to isolate novel NF-κB inhibitors that inhibit DNA binding activity and cancer growth. We also found that DNA binding of transcription factors SP1 and AP1 (c-jun) can be detected by DSE-FRET (data not shown). Therefore, DSE-FRET may be applicable to detection of many DNA-binding proteins.

Acknowledgment

This study was carried out as part of the Project for Development of Innovative Research on Cancer Therapeutics (P-Direct), Ministry of Education, Culture, Sports, Science and Technology of Japan.

Disclosure Statement

H.T. owns stock in MiRTeL Inc. The other authors have no conflict of interest.

References

1 Latchman DS. Transcription factors as potential targets for therapeutic drugs. *Curr Pharm Biotechnol* 2000; **1**: 57–61.
2 Darnell JE Jr. Transcription factors as targets for cancer therapy. *Nat Rev Cancer* 2002; **2**: 740–9.
3 Garner MM, Revzin A. A gel electrophoresis method for quantifying the binding of proteins to specific DNA regions: application to components of the Escherichia coli lactose operon regulatory system. *Nucleic Acids Res* 1981; **9**: 3047–60.
4 Fried M, Crothers DM. Equilibria and kinetics of lac repressor-operator interactions by polyacrylamide gel electrophoresis. *Nucleic Acids Res* 1981; **9**: 6505–25.
5 Galas DJ, Schmitz A. DNAse footprinting: a simple method for the detection of protein-DNA binding specificity. *Nucleic Acids Res* 1978; **5**: 3157–70.
6 Gubler ML, Abarzúa P. Nonradioactive assay for sequence-specific DNA binding proteins. *Biotechniques* 1995; **18**: 1008, 1011–4.
7 Heyduk T, Heyduk E. Molecular beacons for detecting DNA binding proteins. *Nat Biotechnol* 2002; **20**: 171–6.
8 Wang J, Li T, Guo X, Lu Z. Exonuclease III protection assay with FRET probe for detecting DNA-binding proteins. *Nucleic Acids Res* 2005; **33**: e23.
9 Chen Z, Ji M, Hou P, Lu Z. Exo-dye-based assay for rapid, inexpensive, and sensitive detection of DNA-binding proteins. *Biochem Biophys Res Commun* 2006; **345**: 1254–63.
10 Grigoriev M, Hsieh P. A histone octamer blocks branch migration of a Holliday junction. *Mol Cell Biol* 1997; **17**: 7139–50.
11 Prabhu VP, Simons AM, Iwasaki H, Gai D, Simmons DT, Chen J. p53 blocks RuvAB promoted branch migration and modulates resolution of Holliday junctions by RuvC. *J Mol Biol* 2002; **316**: 1023–32.
12 Poulet A, Buisson R, Faivre-Moskalenko C *et al.* TRF2 promotes, remodels and protects telomeric Holliday junctions. *EMBO J* 2009; **28**: 641–51.
13 Takeiri M, Horie K, Takahashi D *et al.* Involvement of DNA binding domain in the cellular stability and importin affinity of NF-κB component RelB. *Org Biomol Chem* 2012; **10**: 3053–9.
14 May MJ, Ghosh S. Signal transduction through NF-kappa B. *Immunol Today* 1998; **19**: 80–8.
15 Sha WC. Regulation of immune responses by NF-kappa B/Rel transcription factor. *J Exp Med* 1998; **187**: 143–6.
16 Barnes PJ, Karin M. Nuclear factor-kappaB: a pivotal transcription factor in chronic inflammatory diseases. *N Engl J Med* 1997; **336**: 1066–71.
17 Sharma RK, Otsuka M, Pande V, Inoue J, João Ramos M. Evans Blue is an inhibitor of nuclear factor-kappaB (NF-kappaB)-DNA binding. *Bioorg Med Chem Lett* 2004; **14**: 6123–7.
18 Umezawa K. Possible role of peritoneal NF-κB in peripheral inflammation and cancer: lessons from the inhibitor DHMEQ. *Biomed Pharmacother* 2011; **65**: 252–9.
19 Yamamoto M, Horie R, Takeiri M, Kozawa I, Umezawa K. Inactivation of NF-kappaB components by covalent binding of (-)-dehydroxymethylepoxyquinomicin to specific cysteine residues. *J Med Chem* 2008; **51**: 5780–8.
20 Panyutin IG, Hsieh P. Formation of a single base mismatch impedes spontaneous DNA branch migration. *J Mol Biol* 1993; **230**: 413–24.
21 Karin M. NF-kappaB as a critical link between inflammation and cancer. *Cold Spring Harb Perspect Biol* 2009; **1**: a000141.
22 Baud V, Karin M. Is NF-kappaB a good target for cancer therapy? Hopes and pitfalls. *Nat Rev Drug Discov* 2009; **8**: 33–40.

Research Article

EASL EUROPEAN ASSOCIATION FOR THE STUDY OF THE LIVER | JOURNAL OF HEPATOLOGY

Reactivation from occult HBV carrier status is characterized by low genetic heterogeneity with the wild-type or G1896A variant prevalence

Tadashi Inuzuka[1], Yoshihide Ueda[1], Hiroki Morimura[1], Yosuke Fujii[1], Makoto Umeda[2], Tadayuki Kou[3], Yukio Osaki[4], Shinji Uemoto[5], Tsutomu Chiba[1], Hiroyuki Marusawa[1,*]

[1]*Department of Gastroenterology and Hepatology, Graduate School of Medicine, Kyoto University, Kyoto, Japan;* [2]*Department of Gastroenterology and Hepatology, Hyogo Prefectural Amagasaki Hospital, Hyogo, Japan;* [3]*Department of Gastroenterology and Hepatology, Kitano Hospital, Osaka, Japan;* [4]*Department of Gastroenterology and Hepatology, Osaka Red Cross Hospital, Osaka, Japan;* [5]*Department of Surgery, Graduate School of Medicine, Kyoto University, Kyoto, Japan*

Background & Aims: Individuals negative for hepatitis B surface antigen (HBsAg) but positive for antibodies to hepatitis B core antigen (anti-HBc) are at risk of hepatitis B virus (HBV) reactivation under immunosuppressive conditions. We investigated clinical features and viral genetics in patients with reactivation from occult HBV infection triggered by chemotherapy or immunosuppressive therapy.

Methods: Clinical courses of 14 individuals originally HBsAg-negative but anti-HBc-positive that experienced HBV reactivation were examined. Ultra-deep sequencing analysis of the entire HBV genome in serum was conducted. Prevalence of the G1896A variant in latently infected livers was determined among 44 healthy individuals that were HBsAg-negative but anti-HBc-positive.

Results: In 14 cases, HBV reactivation occurred during (n = 7) and after (n = 7) termination of immunosuppressive therapy. Ultra-deep sequencing revealed that the genetic heterogeneity of reactivated HBV was significantly lower in patients with reactivation from occult HBV carrier status compared with that in patients from HBsAg carrier status. The reactivated viruses in each case were almost exclusively the wild-type G1896 or G1896A variant. The G1896A variant was detected in 42.9% (6/14) of cases, including two cases with fatal liver failure. The G1896A variant was observed in the liver tissue of 11.4% (5/44) of individuals with occult HBV infection.

Conclusions: Reactivation from occult HBV infection is characterized by low genetic heterogeneity, with the wild-type G1896 or G1896A variant prevalent.

Keywords: G1896A pre-core variant; Genetic heterogeneity; Immunosuppressive therapy; Occult HBV infection; Ultra-deep sequencing.

Received 10 December 2013; received in revised form 7 April 2014; accepted 24 April 2014; available online 4 May 2014

* Corresponding author. Address: Department of Gastroenterology and Hepatology, Graduate School of Medicine, Kyoto University, 54 Kawahara-cho, Shogoin, Sakyo-ku, Kyoto 606-8507, Japan. Tel.: +81 75 751 4319; fax: +81 75 751 4303.
E-mail address: maru@kuhp.kyoto-u.ac.jp (H. Marusawa).

Abbreviations: ALF, acute liver failure; ALT, alanine aminotransferase; anti-HBc, antibodies to hepatitis B core antigen; ETV, entecavir; HBeAg, hepatitis B e antigen; HBsAg, hepatitis B surface antigen; HBV, hepatitis B virus; PCR, polymerase chain reaction; pre-C, pre-core; T-bil, total bilirubin.

Introduction

Clinical features and pathophysiology of hepatitis B virus (HBV) infection are determined by the balance between the host immune response and viral replication. Individuals with persistent HBV infection are at risk of viral reactivation when the host immune system is weakened. HBV reactivation can occur in patients positive for hepatitis B surface antigen (HBsAg) in the serum, under immunosuppressive conditions [1–4]. Evidence has revealed that individuals who are HBsAg-negative but positive for antibodies to hepatitis B core antigen (anti-HBc) can also undergo HBV reactivation, commonly referred to as *de novo* hepatitis B infection, in response to chemotherapy or immunosuppression [5,6]. HBV persists in the liver after the disappearance of HBsAg in individuals with previous exposure to the virus, retaining the serological footprint of anti-HBc positivity, with such a status defined as an occult HBV infection [7,8]. Based on viral transmission studies in living-donor liver transplant patients, we previously demonstrated that most healthy individuals with an occult HBV infection were latently infected by the episomal form of HBV, with ongoing viral replication occurring in the liver [9,10]. Subsequently, we encountered an occult HBV patient with leukemia who developed fatal liver failure caused by viral reactivation [11]. Current guidelines issued by the American Association for the Study of Liver Diseases indicate that immunocompromised patients should undergo testing for HBsAg and anti-HBc before receiving chemotherapy or immunosuppressive therapy; antiviral prophylaxis is recommended for HBV carriers at the onset of chemotherapy or immunosuppression [12]. However, the detailed clinical features and viral genetics of reactivation from occult HBV carrier status are not yet fully understood because of the low incidence of viral reactivation in HBsAg-negative immunocompromised individuals. For example, Hui *et al.* examined the frequency of *de novo* HBV hepatitis among

JOURNAL OF HEPATOLOGY

patients with malignant lymphoma [6]. They reported that 3.3% (8/244) of HBsAg-negative patients receiving rituximab-containing chemotherapy developed HBV reactivation. Moreover, HBV reactivation can also occur only infrequently in HBsAg-negative individuals without hematological malignancies under immunosuppressive conditions [13].

Various mutations in HBV genomes have important implications for sensitivity to antiviral therapy [14,15], and for the pathophysiology of liver diseases. As an example, acute infection with HBV variants containing point mutations at nucleotide 1896 (G1896A) in the pre-core (pre-C) region represents a high risk for developing acute liver failure (ALF) [16–18]. Similarly, predominant reactivation of G1896A variants is frequently observed in HBsAg-positive carriers who develop fatal viral reactivation under immunosuppressive conditions without antiviral prophylaxis [19]. Recent evidence indicates that reactivation from occult HBV infection is of particular concern because the clinical course and outcome of those patients commonly results in severe liver dysfunction and fatal ALF [6], with most fatal cases predominantly containing G1896A pre-C variants [20]. There are an estimated 3 billion individuals who are positive for anti-HBc worldwide, including 10% of the total population in Europe, 15% in the United States, 20% in Japan, and more than 50% in highly endemic areas such as China and Taiwan [21,22]. However, little is known about the prevalence of HBV infection with G1896A pre-C variants among occult HBV carriers, and how reactivation of G1896A pre-C variants leads to fatal consequences.

We examined HBV reactivation in HBsAg-negative and -positive patients. To clarify characteristics of the viral genome and its association with the pathophysiology of HBV reactivation, we used ultra-deep sequencing. This technique allowed for parallel amplification and detection of the full length of the HBV genome for a large number of sequences [23], and assisted in determining the genetic complexity of reactivated viral clones and the prevalence of G1896A pre-C variants.

Patients and methods

Patients and samples

Between April 2007 and July 2013, there were 1377 patients negative for HBsAg and positive for anti-HBc testing (220 patients with hematologic malignancies, 790 patients with solid tumors, and 367 patients with noncancerous diseases), prior to initiation of chemotherapy or immunosuppressive therapy at Osaka Red Cross Hospital, Hyogo Prefectural Amagasaki Hospital, Kitano Hospital, and Kyoto University Hospital. Among them, a total of 14 patients were diagnosed with HBV reactivation and their serum samples were available for further analyses (Table 1). All patients were originally HBsAg-negative but anti-HBc-positive before viral reactivation, and lacked any risk factors for external viral transmission, as demonstrated by the absence of blood transfusion, drug abuse, sexual contact, or blood contact with a known hepatitis virus carrier. No patients were co-infected with hepatitis C virus, hepatitis D virus or human immunodeficiency virus. All patients were longitudinally followed up at 0.5–3-month intervals until analysis (July 2013) or death. ALF was defined as the presence of hepatic encephalopathy and deranged blood coagulation (prothrombin time international normalized ratio >1.5) [24].

Serum samples were obtained at diagnosis of HBV reactivation as demonstrated by the appearance of circulating HBsAg and HBV DNA under immunosuppressive conditions. Serological HBV markers, including HBsAg, antibodies to HBsAg, anti-HBc, hepatitis B e antigen (HBeAg) and antibodies to HBeAg were measured by chemiluminescent enzyme immunoassay (CLEIA; Fuji Rebio, Tokyo, Japan). Serum HBV DNA titer was analyzed using a commercial polymerase chain reaction (PCR) (COBAS Taqman HBV test; Roche, Branchburg, NJ, USA) with a lower detection limit of 2.1 log copies/ml. The level of HBV DNA was retrospectively quantified in eight samples from five patients with reactivation from occult HBV infection.

To examine the genetic heterogeneity and prevalence of G1896A variants, liver tissue was obtained from 45 consecutive healthy donors negative for HBsAg and positive for anti-HBc who underwent hepatectomy for living-donor liver transplantation at Kyoto University from April 1998 to March 2001. Additionally, we examined the reactivated viruses derived from the serum of six patients who had typical serologic characteristics of the inactive HBsAg carrier state before immunosuppressive therapy. These cases were originally HBsAg-positive, while liver function tests were within the normal range before viral reactivation.

The Kyoto University Ethics Committee approved this study, and written informed consent was obtained from all patients. The study was conducted in accordance with the principles of the Declaration of Helsinki.

Sequencing

PCR and direct population Sanger sequencing, ultra-deep sequencing of the HBV genome, sequencing data analysis, and statistical analysis are described in the Supplementary materials and methods.

Data deposition

Sequence reads with Genome Analyzer were deposited in the DNA Data Bank of Japan Sequence Read Archive (http://trace.ddbj.nig.ac.jp/dra/index_e.shtml) under accession number DRA001211.

Results

Clinical features and outcomes of reactivation from occult HBV infection after immunosuppression

Baseline clinical and virological characteristics of 14 patients who developed HBV reactivation under immunosuppressive conditions are summarized in Table 1. All patients were originally HBsAg-negative but anti-HBc-positive before viral reactivation, and had no history of liver dysfunction. Pre-reactivation sera from five patients were available for further analysis, and confirmed that serum HBV DNA was undetectable in the repeated high-sensitivity PCR [10]. Among the 14 patients, 12 cases had hematological malignancy and received chemotherapy with steroids (n = 12) and/or rituximab (n = 7), and with (n = 4) or without (n = 8) hematopoietic stem cell transplantation (Table 1). One patient was diagnosed with psoriasis and had single-agent cyclosporine therapy for 4 years. Another patient had colon cancer and underwent surgery followed by S-1 (Tegafur/gimeracil/oteracil; Taiho Pharmaceutical Co., Tokyo, Japan) adjuvant chemotherapy.

The median time between initiation of chemotherapy or immunosuppressive therapy and diagnosis of HBV reactivation was 15.6 months (range: 1.0–57.7 months) (Table 1). Viral reactivation in seven of the 14 cases occurred 9.5 months (median; range: 6.4–39.8 months) after termination of chemotherapy or immunosuppressive therapy, while the remaining seven cases developed HBV reactivation during chemotherapy or immunosuppressive therapy. Median serum alanine aminotransferase (ALT) levels and HBV DNA levels at the time of HBV reactivation were 652 IU/ml [range: 15–2028] and 6.6 log copies/ml [range: 5.0–9.0], respectively (Table 2).

All patients except case #5 were treated with entecavir (ETV) (0.5 mg, once daily) immediately after diagnosis of HBV reactivation to suppress viral activity (Table 2). Representative clinical courses of patients with reactivation from occult HBV infection are shown in Fig. 1. Four of 14 patients (cases #2, #6, #9, and #11) got tested for HBV markers at 1–3 months intervals and started the ETV treatment after HBV DNA appearance (Table 2). The remaining ten patients were diagnosed with HBV reactivation

Research Article

Table 1. Clinical characteristics of patients with reactivation from occult HBV and HBsAg carrier status BEFORE viral exacerbation.

Case	Age/ sex	Anti-HBs	Primary disease	Treatment	Use of steroids	HSCT	Period between HBV reactivation and start of treatment (months)	Period between HBV reactivation and end of treatment (months)
Reactivation from occult HBV carrier status								
#1	48M	+	ML	Fludarabine	+	+	57.7	39.8
#2	25M	-	AML	IDA + AraC	+	+	27.0	19.2
#3	59M	Unknown	Colon cancer	S-1	-	-	3.6	During treatment
#4	61M	Unknown	ML	R-CHASE	+	+	13.8	9.5
#5	64M	-	MM	MP→CAD	+	+	13.6	6.4
#6	72M	-	ML	MTX + AraC →Rituximab	+	-	10.9	During treatment
#7	78M	Unknown	ML	R-CVP	+	-	34.7	34.2
#8	66M	Unknown	MM	MP	+	-	49.1	6.6
#9	61F	-	ML	R-FND	+	-	1.0	During treatment
#10	66M	Unknown	Psoriasis	Cyclosporine	-	-	37.8	During treatment
#11	79F	Unknown	ML	R-CHOP	+	-	3.7	During treatment
#12	81F	-	ML	R-CVP	+	-	11.2	7.6
#13	84F	Unknown	ML	R-CHOP	+	-	17.4	During treatment
#14	87F	+	MM	MP	+	-	23.1	During treatment
							median: 15.6	**median: 9.5**
Reactivation from HBsAg carrier status								
#15	32F	-	Sjögren synd.	PSL	+	-	15.1	During treatment
#16	63F	-	Raynaud's dis.	PSL	+	-	20.4	During treatment
#17	42F	-	Aortitis synd.	PSL	+	-	122.2	During treatment
#18	59M	-	Lung cancer	Chemotherapy[a]	+	-	17.9	During treatment
#19	54M	-	RA	MTX + PSL	+	-	11.5	During treatment
#20	72M	-	RA	Bucillamine	-	-	6.7	During treatment
							median: 16.5	

[a]Carboplatin, paclitaxel → docetaxel → gemcitabine, vinorelbine → cisplatin, irinotecan.
AML, acute myeloid leukemia; AraC, cytarabine; dis, disease; CAD, cyclophosphamide, doxorubicin, dexamethasone; F, female; HBsAg, hepatitis B surface antigen; HSCT, hematopoietic stem cell transplantation; IDA, idarubicin; M, male; ML, malignant lymphoma; MM, multiple myeloma; MP, melphalan, prednisolone; MTX, methotrexate; PSL, prednisolone; RA, rheumatoid arthritis; R-CHASE, rituximab, cyclophosphamide, cytosine arabinoside, etoposide, dexamethasone; R-CHOP, rituximab, cyclophosphamide, doxorubicin, vincristine, prednisolone; R-CVP, rituximab, cyclophosphamide, doxorubicin, prednisolone; synd, syndrome; R-FND, rituximab, fludarabine, mitoxantrone, dexamethasone.

when they had elevated levels of serum ALT and ETV was given in these cases (except case #5) after the appearance of liver dysfunction. After administering ETV, serum HBV DNA levels decreased in 11 cases (excluding cases #13 and #14), accompanied by reduced serum ALT levels. Nine (69.2%) of these cases showed loss of HBsAg with the appearance of anti-HBs at a median time of 2.9 months (range: 0.6–13.5 months) following the commencement of ETV treatment (Table 2). After confirming stable HBsAg/anti-HBs seroconversion, ETV was stopped in three of nine cases after 15.2 months (mean; range: 6.8–26.8 months). The four cases without HBsAg disappearance included two cases (#6 and #8) with follow-up of <3 months after ETV administration, and two cases (#13 and #14) that developed fatal ALF before complete disappearance of HBsAg. When the latter two were diagnosed with HBV reactivation, liver function had already deteriorated (serum total bilirubin (T-bil) was 8.0 mg/dl for #13 and 2.3 mg/dl for #14) and they died of liver failure 33 (#13) and 16 days (#14) after ETV administration.

Low heterogeneity of the reactivated viruses in patients with reactivation from occult HBV infection

To identify characteristics of viral clones related to HBV reactivation, we determined the entire virus genome sequence using ultra-deep sequencing. We first conducted a control experiment to validate the efficacy and errors in the sequencing platform. We determined two full-length plasmid-derived HBV sequences using expression plasmids encoding wild-type HBV as a template. Sequencing generated 1,229,416 and 2,205,237 filtered reads, corresponding to a mean coverage of 34,026 and 61,504 fold at each nucleotide site. The mean nucleotide mismatch error rate was 0.038% in Control #1 and 0.015% in Control #2, with the distribution of per-nucleotide error rate 0–0.24% and 0–0.16%, respectively; the mean overall error rate was 0.45% and 0.26%, respectively (Supplementary Table 1). This reflected the error introduced by sequencing. We defined the cut-off value in the current platform as 1% to exclude mismatch errors and to detect low-abundance mutations.

We then conducted ultra-deep sequencing on samples from the 14 patients with reactivation from occult HBV infection. A mean of 605,890 reads were mapped onto the reference sequences, and a mean coverage depth of 16,712 bp was achieved for each nucleotide site of HBV sequences (Table 3). The frequency of the overall mismatch mutations, which were nucleotides that did not match to the reference sequences, was 0.015% (15/100,000).

To define the characteristics of the reactivated HBV clones, we compared these clones with those derived from reactivated

Table 2. Clinical courses of patients with reactivation from occult HBV and HBsAg carrier status AFTER viral exacerbation.

Case	At diagnosis of HBV reactivation				ETV treatment*	Period to HBsAg disappearance** (months)
	HBV genotype	HBeAg/ anti-HBe	HBV DNA level (log_{10} copies/ml)	ALT[a] level (IU/ml)		
Reactivation from occult HBV carrier status						
#1	C	+/-	8.2	1915	+	13.3
#2	C	+/-	6.2	24	+	2.8
#3	C	+/-	6.4	2019	+	0.6
#4	C	+/-	8.3	720	+	3.1
#5	C	+/-	5.4	681	n.t.	-
#6	C	+/-	8.4	15	+	-
#7	B	+/-	7.7	1983	+	2.9
#8	B	+/-	6.2	97	+	-
#9	C	-/+	5.0	18	+	1.7
#10	C	-/+	6.6	2028	+	0.9
#11	C	-/+	5.4	38	+	13.5
#12	B	-/+	9.0	503	+	10.5
#13	B	-/+	6.5	623	+	-
#14	B	-/+	8.5	705	+	-
			median: 6.6	**median: 652**		**median: 2.9**
Reactivation from HBsAg carrier status						
#15	C	+/-	8.8	499	+	-
#16	C	+/-	7.1	1740	+	-
#17	C	-/+	7.8	628	+	-
#18	C	-/+	5.5	1674	+	-
#19	B	-/+	5.8	619	+	-
#20	C	-/+	8.8	813	+	0.4
			median: 7.5	**median: 716**		

ALT, alanine aminotransferase; anti-HBe, antibodies to hepatitis B e antigen; ETV, entecavir; HBeAg, hepatitis B e antigen; HBsAg, hepatitis B surface antigen; HBV, hepatitis B virus; n.t., not treated.

*All patients except case #5 were treated with ETV immediately after diagnosis of HBV reactivation to suppress viral activity.

**Period (months) between ETV administration and HBsAg disappearance a normal range 10–42 IU/L.

viruses in six cases originally positive for HBsAg who developed viral exacerbation triggered by immunosuppressive therapy. There were no significant differences in the maximum levels of elevated serum ALT and HBV DNA during viral exacerbation between the both groups (Table 2). A mean of 630,253 reads for HBV sequences derived from patients with reactivation from HBsAg carriers were mapped onto reference sequences (Table 3). The overall mismatch mutation frequency of total viral genomic sequences was 0.11% (114/100,000), suggesting that viral heterogeneity was significantly lower in the reactivated viruses from occult HBV infection (0.015%) compared with HBsAg carriers (p <0.05) (Fig. 2A–C and Table 3). Viral heterogeneity was also evaluated by calculating Shannon entropy values. The mean overall value of Shannon entropy was 0.00085 (range: 0–0.0022) in patients with reactivation from occult HBV infection, and 0.0051 (range: 0.0006–0.017) in patients with reactivation from HBsAg carriers, indicating that genetic complexity was significantly lower in the reactivated viruses from occult HBV carrier status (p <0.05) (Fig. 2D). These findings suggest that the heterogeneity of reactivated HBV was substantially smaller in originally HBsAg-negative cases than in HBsAg-positive carriers. The levels of heterogeneity were not significantly different between the viral genomic regions, and no significant increase in the population of immune escape variants in both the patients with reactivation from occult HBV and HBsAg carrier status (Fig. 2A and B, and Supplementary Fig. 1).

Reactivated viruses in each individual consisted almost exclusively of the wild-type G1896 or G1896A variant

The G1896A mutation in the pre-C region is associated with ALF, and is one of the most commonly shared features in patients with HBV reactivation and ALF [16–19]. We found that six of 14 patients, including two fatal ALF cases, had predominant reactivation of variant G1896A pre-C clones. Serologically, all cases with the dominant G1896A pre-C variant were negative for HBeAg and positive for anti-HBe at the time of HBV reactivation (Tables 2 and 4). Almost all the reactivated viral clones in the G1896A-dominant cases were G1896A pre-C variant clones (99.4–100%). Very few clones with the wild-type G1896 sequence were detectable by ultra-deep sequencing at the time of HBV reactivation (Table 4). Ultra-deep sequencing also confirmed that patients with reactivation of the wild-type G1896-dominant HBV clones had few or no G1896A pre-C variants in their serum (0–0.9%). These findings indicate that either wild-type G1896 or G1896A pre-C variants were exclusively reactivated in patients with reactivation from occult HBV infection following immunosuppression. We also examined whether the G1896A pre-C

Research Article

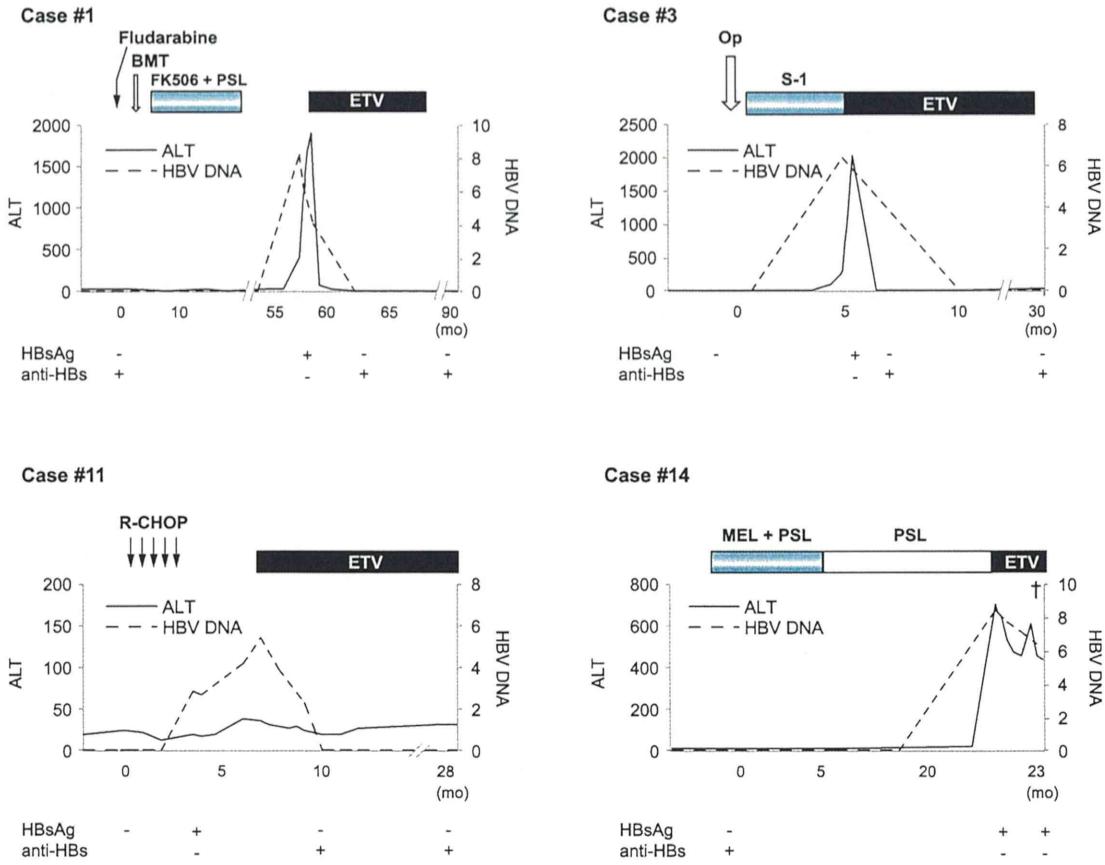

Fig. 1. Representative clinical courses of patients with reactivation from occult HBV infection. Serial serum ALT, HBV DNA and HBV serology of four cases that developed HBV reactivation after (cases #1) or during (cases #3, #11 and #14) chemotherapy or immunosuppressive therapy. All cases were treated with entecavir (ETV) immediately after diagnosis of HBV reactivation. BMT, bone marrow transplantation; FK506, tacrolimus; MEL, melphalan; Op, operation; PSL, prednisolone; R-CHOP, rituximab, cyclophosphamide, doxorubicin, vincristine, prednisolone.

variant or the level of heterogeneity was associated with the clinical course. We found no significant association between the ratio of the wild-type/G1896A pre-C mutant or the heterogeneity (represented by the Shannon entropy value) and the levels of peak ALT and peak T-bil (Supplementary Fig. 2). The predominance of A1762T and G1764A variants in the core-promoter region, which are known to be associated with ALF [18,25], was observed in only two cases (#9 and #11), and was not associated with the two fatal ALF cases (Table 4).

To clarify the genomic similarity between the viral clones in the liver tissue before reactivation and those in the serum after reactivation, we determined the sequences of HBV genomes in liver tissue before the onset of HBV reactivation in a patient (case #3). The patient was initially negative for HBsAg but positive for anti-HBc, and had colon cancer and liver metastasis. He underwent partial hepatectomy, followed by adjuvant chemotherapy. During cancer treatment, he became seropositive for HBV DNA and HBsAg (Fig. 1). We compared the HBV genome sequences derived from the liver before viral breakthrough (obtained at the time of hepatectomy) with those from his serum at the time of viral reactivation during chemotherapy. We found that 97.9% of the HBV nucleotides derived from his serum at reactivation were identical to those from the liver tissues before viral reactivation. The prevalence of the wild-type G1896 strain was 99.95% in liver prior to reactivation, and 99.94% in serum after reactivation. These results possibly indicate that the viral population in the serum of a patient with reactivation from occult HBV infection was similar to that in the liver tissue during latent infection before viral breakthrough.

Based on those findings, we determined the prevalence of the G1896A variant in the liver of occult HBV carriers that did not experience immunosuppression. We examined the liver tissues of HBsAg-negative but anti-HBc-positive healthy donors used for living-donor liver transplantation. The HBV genome was detectable by PCR in the livers of most (44/45) of the healthy donors that lacked circulating HBV DNA. Ultra-deep sequencing determined viral genome sequences with a mean 20,503-fold coverage at each nucleotide site for each liver specimen. Sequencing revealed that the viral clones comprised almost exclusively of the wild-type G1896 or G1896A pre-C variant in the livers of occult HBV carriers. Around 11.4% (5/44) of cases had a dominant population of the G1896A pre-C variant, with a frequency of >99.9% for total viral clones (Fig. 3). Approximately 88.6% (39/44) of cases predominantly contained the wild-type G1896 strain, with 38/39 cases (liver #6 was the exception) exhibiting a frequency of >99.9% of total viral clones (Fig. 3).